12-2010

A synthetic analysis of integrated data fusion: Combining hydrologic and geophysical data collected during a tracer test to estimate aquifer flow and transport parameters

Dylan Fowler
Clemson University, DylanFowler@aol.com

A SYNTHETIC ANALYSIS OF INTEGRATED DATA FUSION: COMBINING HYDROLOGIC AND GEOPHYSICAL DATA COLLECTED DURING A TRACER TEST TO ESTIMATE AQUIFER FLOW AND TRANSPORT PARAMETERS

A Thesis
Presented to
the Graduate School of
Clemson University

In Partial Fulfillment
of the Requirements for the Degree
Master of Science
Hydrogeology

---

by
Dylan Erwin Fowler
December 2010

Accepted by:
Stephen Moysey, Committee Chair
Lawrence Murdoch
Taufiquar Khan

ABSTRACT

Integrated data fusion (IDF), also known as coupled inversion, is becoming a more widely used method for estimating hydrologic parameters from geophysical data. IDF is being used in this research as an approach to inversion that couples mathematical models of groundwater flow, solute transport, and electrical resistivity for the direct estimation of hydraulic conductivity, porosity, and dispersivity from transient resistivity data collected during a tracer test. In this work, synthetic field resistivity data are generated using only a single current electrode pair and many potential electrodes. This data is then used within the IDF framework to a) estimate hydraulic conductivity with a gradient-based optimization algorithm, b) analyze trends in hydraulic conductivity estimates related to changes in environmental and survey conditions, c) analyze model sensitivity to changes in hydraulic conductivity, porosity, and dispersivity, and d) determine if the limited resistivity data utilized are enough to infer that the initial conceptual model was incorrect. The results of the simulations indicate that hydraulic conductivity and porosity can be constrained quite well if Archie's Law is known, but dispersivity may remain non-unique due to trade-offs with velocity and the spatial distribution of the plume. In addition, there may not be enough information contained within current/potential pair data to definitively rule out the possibility that the system is homogeneous; therefore the addition of more current pairs may be necessary.

DEDICATION

For my Mother, Father, Scott, and Walter whose patience and encouragement has been a constant positive force throughout my graduate career.

TABLE OF CONTENTS

LIST OF TABLES

LIST OF FIGURES

CHAPTER 1

INTRODUCTION

1.1 Overview

Determination of hydrologic parameters, primarily physical properties controlling groundwater flow and transport, is an important aspect of aquifer characterization. There are many methods for estimation of these parameters such as well tests (slug and pumping) and tracer tests which, in many cases, utilize direct measurements taken while stressing the aquifer. These traditional methods require many subsurface sampling locations in the form of boreholes which can be costly to install and monitor. If wells are already installed, the direct methods are a rapid way to attain flow characteristics of an aquifer. Although flow characteristics can be easily gleaned using standard hydrogeological borehole methods, transport characteristics are much harder to attain as is the case of a tracer test, where the migrating plume can be missed by the sampling locations altogether.

One alternative that could possibly reduce drilling costs and that has the potential for a higher spatial sampling density is geophysical methods. Geophysical methods such as electrical resistivity tomography (ERT) use non-invasive indirect measurements to map or image geophysical parameters. However, characterization of aquifer transport properties from geophysical data is challenging. One must first process the geophysical data to obtain transient hydrologic state data and then use this information to obtain hydrologic parameter estimates. This workflow, which is sometimes referred to as

sequential data fusion (SDF) [Moysey et al., 2006] has been the primary method for inverting hydrogeophysical data for the purpose of aquifer flow and transport characterization [Hinnell et al., 2010; Huisman et al., 2010]. SDF is often inefficient and can sometimes lead to erroneous results because of the underdetermined (i.e. lack of sufficient data to produce unique estimates) nature of the inversion [Singha and Gorelick, 2005].

An alternative to SDF, called integrated data fusion (IDF) couples models for groundwater flow and transport with a model for electrical resistivity. By interpreting geophysical data in a multiphysics model environment, geophysical imaging steps needed for SDF inversion can be bypassed. This research investigating IDF is meant to answer these questions:

- Can IDF be used to estimate hydraulic conductivity from resistivity data collected during a tracer test, and under what environmental conditions could this estimation be successful?
- What is the sensitivity of electrical resistivity data to hydraulic conductivity (K), porosity (n), and dispersivity (α), and how will that sensitivity affect the ability to estimate these parameters?
- What are the risks and consequences if the initial hydrologic conceptual model used as a constraint in IDF is wrong?

To answer these questions an idealized synthetic model has been constructed that couples groundwater flow, solute transport, and electrical resistivity using the finite

element software COMSOL Multiphysics [COMSOL, 2006; COMSOL 2008]. The model will simulate transient resistivity data collected during a tracer test, and then be used to analyze model sensitivity to various flow and transport parameters. Model design and environment conditions are also investigated. The purpose of using an idealized case is to allow for only the hydrologic parameters of interest to impact the model output (e.g. voltage or resistivity data), thus providing insight into the capability of IDF to constrain the hydrologic problem using only electrical resistivity. To take data sparsity to an even more extreme level, the model only includes one current electrode pair, but many potential electrodes. The use of only one current pair will allow for more rapid data collection during the saline tracer's movement across the model domain, giving insight into potential of low-cost resistivity monitoring arrays that use a limited number of electrodes.

1.2 Summary

The following research tasks have been completed:

1. *Deterministic, gradient-based estimation of hydraulic conductivity and an objective function analysis to determine sensitivity of hydraulic conductivity estimation to changes in environmental conditions (Chapter 2):* A straightforward synthetic evaluation in three dimensions has been conducted which links hydraulic conductivity to observed voltages by using coupled forward models for groundwater flow, solute transport, and electrical current flow in COMSOL Multiphysics. This was a deterministic evaluation of hydraulic

conductivity, therefore only the parameter estimate was considered with no regards to the uncertainty involved. Also, for the purpose of taking into account the possible uncertainty involved in the parameter estimation, an objective function sensitivity analysis in two dimensions (i.e. 2-D simulations of flow and transport) was conducted using a range of hydraulic conductivity values and variable injection concentration, background noise, and injection depth. This analysis was conducted to determine the expected trends in goodness of fit considering the relative changes in environmental variables.

2. *Objective function analysis to determine sensitivity to changes in hydraulic conductivity, porosity, and dispersivity (Chapter 3):* An objective function analysis was conducted with variations in hydraulic conductivity, porosity, and the dispersivity tensor. The 3D model links an analytical solution for groundwater flow and solute transport in MATLAB to electrical current flow in COMSOL Multiphysics. This analysis was conducted to determine whether the transport parameters could be uniquely determined from resistivity data in an IDF model calibration. This chapter has been submitted for publication to Journal of Hydrology.
3. *Analysis of consequences related to an incorrect initial conceptual model hypothesis (Chapter 4)*: Using synthetic data generated in systems with two hydraulic conductivity zones (diametrically opposite systems that force the tracer away from and towards the surface), a manual fit of the apparent resistivity signal is conducted using a homogeneous model design. An objective function analysis

is also conducted to determine IDF's capability to estimate *K* in a block that represents a low-*K* zone (similar to a no-flow zone) relative to the background subdomain. The model links hydraulic conductivity, porosity, and dispersivity to electrical resistivity by using coupled forward models for groundwater flow, solute transport, and electrical current flow in COMSOL Multiphysics. This analysis was conducted for the purpose of demonstrating how conceptual model error could lead to a misinterpretation of aquifer properties using IDF as the inversion strategy.

1.3 Implications of this Research

This research will primarily benefit the fields of high-resolution aquifer characterization and geophysical site assessments. Improved characterization will, for example, assist hydrogeologists in developing monitoring and remediation plans for contaminated sites.

1.4 References

Comsol Multiphysics 3.3a: User's Guide (2006), www.comsol.com.

Comsol Multiphysics 3.5a: User's Guide, (2008), www.comsol.com.

Hinnell, A. C. , T. P. A. Ferre, J. A. Vrugt, J. A. Huisman, S. Moysey, J. Rings, M. B. Kowalsky (2010), Improved extraction of hydrologic information from geophysical data through coupled hydrogeophysical inversion, *Water Resources Research*, vol. 46, W00D40.

Huisman, J. A, J. Rings, J.A. Vrugt, J. Sorg, H. Vereecken (2010), Hydraulic properties of a model dike from coupled Bayesian and multi-criteria hydrogeophysical inversion, *Journal of Hydrology*, vol. 380, pp. 62–73.

Moysey S., R. J. Knight, K. Singha (2006), Relating geophysical and hydrologic properties using field-scale rock physics, *CMWR XVI -- Computational Methods in Water Resources*, Copenhagen, Denmark, 8p.

Singha, K., S. M. Gorelick (2005), Saline tracer visualized with three-dimensional electrical resistivity tomography: Field-scale spatial moment analysis, *Water Resources Research*, vol. 41, W05023.

CHAPTER 2

A SYNTHETIC EVALUATION OF INTEGRATED DATA FUSION: ESTIMATION OF HYDRAULIC CONDUCTIVITY USING RESISTIVITY DATA COLLECTED DURING A TRACER TEST

2.1 Abstract

Integrated data fusion (IDF), or coupled inversion, is becoming a more widely used method for estimating hydrologic parameters from geophysical data. This research tests the ability of IDF to estimate hydraulic conductivity using electric potential data collected during a tracer test in a homogeneous aquifer. In this work, synthetic field resistivity data are generated and used to estimate hydraulic conductivity with a gradient-based optimization algorithm. In addition to the simple parameter estimation, a sensitivity analysis was conducted to determine what trends may arise in the estimation of hydraulic conductivity in relation to changes in specific environmental and survey conditions (tracer concentration, tracer injection depth, and noise in voltages). The numerical simulations indicate that resistivity data can be used within the IDF framework to provide good estimates of aquifer hydraulic conductivity for a variety of conditions.

2.2 Introduction

Tracer tests have been utilized for decades as a means to characterize subsurface transport processes [Molz et al., 1985; Sudicky, 1986; Feehley et al., 2000]. Despite their benefits, tracer tests also have some key limitations. In particular, tracer tests require

sampling of the tracer at borehole locations. Often, this causes the test to be costly, invasive, and have a low spatial and temporal sampling density, which can result in under-sampling of the migrating plume. Geophysical methods, such as surface-based electrical resistivity surveys, can provide a cost-effective, minimally invasive alternative. The benefits of employing resistivity include:

- Reducing the disturbance of the subsurface
- Having a higher spatial sampling density
- Increasing the extent of the subsurface sampled
- Reducing the labor for sampling
- Being a low cost alternative

Despite the advantages, there are drawbacks with traditional geophysical imaging schemes that cause difficulty with the interpretation of hydrologic processes. The most direct approach to integrating geophysical data in a hydrologic estimation problem is Sequential Data Fusion (SDF). The SDF workflow consists of: 1) collection of resistivity data, 2) inversion to produce a resistivity image of the subsurface, 3) application of rock physics relationships to convert the resistivities to produce a concentration image, and 4) inversion of the resulting geophysically-based concentration data to hydraulic parameters. Difficulties sometimes arise in SDF. For example, upscaling from core-scale to field-scale rock physics relationships must be considered [Moysey et al., 2005] as the interactions between electrical measurements and spatial heterogeneity at the field-scale cannot be reproduced in the lab. Averaging and inversion artifacts can produce resistivity images that are smoothed representations of the true subsurface; this is particularly

problematic when limited data are available and extreme resistivity values are of interest – such as when monitoring a transient tracer test. SDF can also be computationally laborious especially when stochastic estimation methods are to be used, because of the hundreds or thousands of images that must be produced in both the geophysical and hydrologic inversion to quantify the uncertainty involved.

The interpretation strategy utilized in this research, Integrated Data Fusion (IDF) [Moysey et al., 2006] or closed-loop inversion [Lambot et al., 2006] is a physics-based regularization that links a hydrological model to geophysical data and directly estimates hydraulic parameters. It is hypothesized that IDF can be utilized with resistivity data for improved estimation of flow and transport parameters of the aquifer. IDF can be used to improve parameter estimates and to circumvent the above SDF steps by applying prior knowledge about the physics of subsurface hydrogeologic processes. The multiphysics model and a parameter estimation algorithm are then used to hone in on the best estimate of the hydraulic conductivity. This method allows for use of *a priori* information in the determination of model geometry and then directly estimates the parameters of interest (e.g. K) without undergoing the additional steps of traditional geophysical inversion. IDF also has the potential to avoid the underdetermined nature of many geophysical inverse problems (i.e. estimation of hundreds or thousands of parameters using a limited amount of data) by directly estimating fewer transport parameters controlling the state of the subsurface.

The IDF method (Figure 2.1) consists of multiphysics simulation that couples hydrologic and geophysical models. Hydrologic parameters to be estimated (i.e., K) are

input into the hydrologic simulation module that outputs state variables such as concentration. Using rock physics relationships, the hydrologic properties are converted to geophysical properties. In this research, Archie's Law is used to convert fluid solute concentration to effective electrical resisitivity. The geophysical properties are then input into the geophysical simulation module to produce the simulated data in the form of electric potential (i.e. voltages) at the ground surface. The difference, or data misfit, between the simulated and field data sets is then used to determine if a stopping criteria threshold has been exceeded. If not, then the hydrologic parameters are updated and the simulation is run again. If the stopping criteria have been met, the parameter estimation is ended with the final hydrologic parameter estimates as the output.

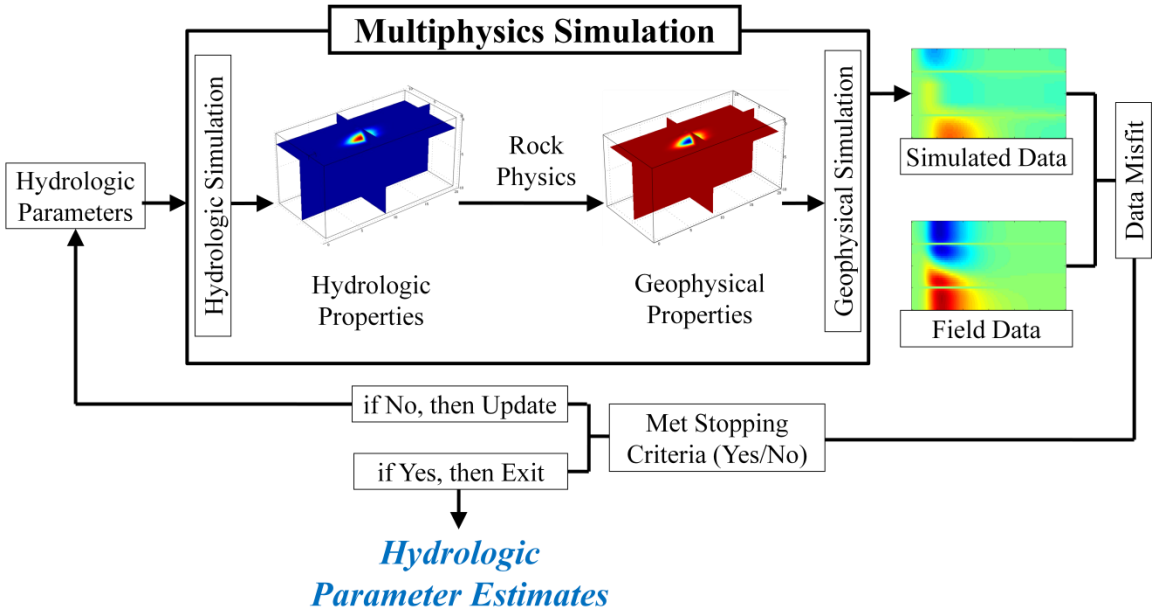

Figure 2.1: Flow schematic describing the integrated data fusion (IDF) workflow. The hydrologic and geophysical simulations, coupled by rock physics relationships, comprise the multiphysics simulation. Hydrologic parameters are the input and simulated geophysical data are output of the multiphysics simulation. The simulated geophysical data and field data are then used to compute the model data misfit. If a maximum misfit threshold condition is met, the hydrologic parameter estimates are output.

The main objective of this research is to test the hypothesis that resistivity monitoring data collected during a natural gradient tracer test can be used to constrain the hydraulic conductivity of a homogeneous aquifer using an IDF interpretation strategy. Unlike typical geophysical estimation problems, voltage data are used to directly estimate transport parameters (i.e. hydraulic conductivity). Furthermore, this study considers only one current electrode pair and a limited number of potential electrodes. This sparse data arrangement is not ideal for traditional resistivity imaging surveys where current is typically applied for hundreds of different electrode combinations to sample the subsurface in many different ways. However, dealing with spatial data sparsity is a problem that is likely to become increasingly important for real-time monitoring of dynamic processes where a high temporal sampling frequency is required. Two key problems are addressed in this work: (i) the ability of standard gradient-based optimization schemes to accurately estimate hydraulic conductivity based on observed voltages is assessed, and (ii) the sensitivity of hydraulic conductivity estimates to environmental conditions, such as tracer concentration, injection depth, and noise, is evaluated. Together these analyses provide an initial evaluation of the practicality of using resistivity monitoring of tracer tests to estimate aquifer properties.

2.3 Background

Traditionally, methods for determination of the flow parameters on a field-scale have incorporated a perturbation of the aquifer within or around a well. Slug tests are commonly utilized to rapidly estimate K in the vicinity of the well-bore [Hvorslev, 1951,

Bouwer and Rice, 1976 and Bouwer, 1989]. Constant rate pumping tests are another method frequently used to estimate *K* and include the well-known Theis [Theis, 1935] and Jacob methods [Jacob, 1940]. Though these analyses are generally computationally efficient methods for determination of *K*, they assume that the aquifer is homogeneous, and consequently estimated *K* may not be equivalent to the actual *K* at a distance from the location of the well.

One of the most widespread methods for delineation of groundwater transport parameters in heterogeneous media is a tracer test. Field-scale research utilizing tracer tests to estimate hydraulic parameters includes the Mobile Site experiments [Molz et al, 1985], the Borden experiments [Sudicky, 1986], and the Macro Dispersion Experiment (M.A.D.E) [Feehley et al., 2000]. Though these experiments yielded promising results for estimation of transport parameters at a large-scale (i.e. *K*, α), there continue to be concerns related to the limited observational capabilities of borehole sampling in a heterogeneous environment with respect to small-scale heterogeneities [Molz et al., 1985; Sudicky, 1986]. This restriction of sampling only at the borehole locations often leads to the outright exclusion of the smaller-scale heterogeneities in the transport models [Fitts, 1996]. Thus, when there is a necessity for high spatial resolution in the estimates for devising monitoring and remediation strategies, some form of cross-borehole or ground-surface geophysical data acquisitions may be desired.

Though there are numerous methods for estimating groundwater flow and transport parameters, such as standard down-hole hydrogeological methods (i.e. slug tests and pumping tests) and tracer tests, coupling the standard down-hole data with surface

and/or borehole geophysical data can provide the researcher with the greatest spatial resolution. One low cost, high spatial resolution, minimally invasive alternative to the standard methods for monitoring a tracer test is employment of a geo-electrical method, such as electrical resistivity tomography (ERT) [Daily et al., 1992; Slater et al., 2000; Binley et al., 2002; Kemna et al., 2002].

ERT exploits the relationship between the resistivity of geologic materials and pore fluids in the form of an electrical response at a series of electrodes when an electrical current is injected into the subsurface. The link between solute concentrations and bulk resistivity are described by Archie's Law [Archie, 1942], an empirical relationship first developed use in petroleum reservoir rocks (sandstones). Though Archie's Law can sometimes be unsuitable because it was devised for use at a local, borehole-scale and does not take into account for spatial variability in resolution [Singha and Gorelick, 2006], it is commonly used to relate solute concentration and bulk electrical resistivity. Archie's Law, states that the bulk resistivity of a rock (ρ_b), is affected by porosity (ϕ), fluid saturation (S), and fluid resistivity (ρ_w) [Knight and Endres, 2005]:

$$\rho_b = a\phi^{-m} S^{-n} \rho_w + \rho_g \,. \tag{2.1}$$

The connectivity of fluid in the pore spaces is accounted for by the coefficients m and n, whereas conduction related to the mineral phase is accounted for by the grain resistivity (ρ_g). The coefficient a is an empirical scaling factor.

By utilizing the empirical relationship given by Archie's Law, apparent resistivity images obtained from ERT surveys can be transformed to solute concentrations.

Investigations of this nature have been conducted using tracer tests that track the movement and spatial distribution of a saline tracer [Slater et al., 2000; Singha and Gorelick, 2005 and 2006]. Using Archie's Law in these studies, resistivity data were collected and inverted to produce the concentration profiles in the form of images or breakthrough curves. In the next step, the inverse workflow, though not utilized in these studies, a transport model is optimized to determine the flow and/or transport characteristics. This method of data inversion, which is called sequential data fusion (SDF), follows an indirect path to the parameters of interest and typically requires the estimation of many hundreds or thousands of parameters other than the ones of interest.

IDF for hydrogeophysical estimation [Rucker and Ferre, 2004; Kowalsky et al., 2004 and 2005; Lambot, et al., 2006; Looms et al., 2008; Hinnell et al., 2010; Huisman et al., 2010] is a physics and model-based regularization tool that uses geophysical data to calibrate a hydrologic model and update the parameter estimate until a desired data misfit threshold is reached (Figure 2.1). This new approach has been utilized to estimate hydrologic parameters from ground-penetrating radar tomography data [Rucker and Ferre, 2004; Kowalsky et al., 2004 and 2005] and ERT data [Lambot, et al., 2006; Looms et al., 2008; Hinnell et al., 2010; Huisman et al., 2010]. Of particular interest to this research is ERT monitoring of saline tracer migration. Looms et al. [2008] showed that vadoze-zone hydraulic conductivity could be successfully estimated in one- and two-dimensions using the IDF inversion framework to analyze ERT data collected during a field-scale infiltration test.

2.4 Methods

2.4.1 Model Description

The finite element software COMSOL Multiphysics [COMSOL, 2006a] is used to model the coupled flow, transport, and electrical resistivity simulations in this study. The three-dimensional simulation domain is rectangular with dimensions of L_x = 20m, $L_y = L_z$ = 10m. The Darcy's Law and Solute Transport modules from COMSOL's Earth Science package are used to solve the groundwater flow and solute transport problems, respectively. The DC Electrical Conductivity module is used to simulate the voltage distributions for the electrical resistivity surveys. For simplicity, there is no vadose zone included in the model and as such the model best represents a case where the water table is near the ground surface or where the electrodes protrude into the saturated zone.

2.4.2 Flow and Transport Simulations

The transport scenario investigated in this research is a three-dimensional homogenous aquifer with a uniform, steady-state flow field (Figure 2.2). Groundwater flow in this scenario is governed by the Laplace equation

$$K\nabla^2 h = 0, \tag{2.2}$$

where K is the hydraulic conductivity and h is hydraulic head. Zero flux boundaries are imposed on all surfaces parallel to the flow and specified head boundaries are specified perpendicular to the flow to create a fixed hydraulic gradient along the x-axis of 1m/m. The flow is therefore one dimensional along the x-axis.

Transient solute transport is governed by the advection-dispersion equation [Bear, 1979]

$$\frac{\partial C}{\partial t} = \mathbf{D}\nabla^2 C - v\nabla C\,, \tag{2.3}$$

where C is solute concentration, **D** is the dispersion coefficient tensor, and v is the flow velocity. The dispersion coefficient along the direction j is given by $D_j = \alpha_j v + D_d$ where α_j is the dispersivity and D_d is the molecular diffusion coefficient. In this study the longitudinal, transverse horizontal and transverse vertical dispersivities were fixed to 0.1, 0.01, and 0.001m, respectively. Transport is coupled to the flow field through the velocity, which is determined by means of Darcy's Law [Darcy, 1856]. The average linear velocity, given by Equation 2.4 [Fetter, 2001], accounts for the effective porosity (n_e) which in this study was fixed to 0.3,

$$v = \frac{-K\nabla h}{n_e}\,. \tag{2.4}$$

The solute plume for the tracer test is released from a 1m x 1m x 0.1m patch with a uniform initial concentration of 29g/L. Throughout the rest of the domain, the initial concentration in the model is set to 146mg/L and a constant flux of this same concentration is applied along the upstream boundary to maintain this background value throughout the simulation. The downstream face is set as an advective flux boundary and the top surface of the model is fixed as a zero flux boundary to represent the top of the aquifer. The remaining side faces and bottom of the domain are specified as dispersive flux boundaries to allow mass to escape freely if the plume edge intersects the boundary.

a)

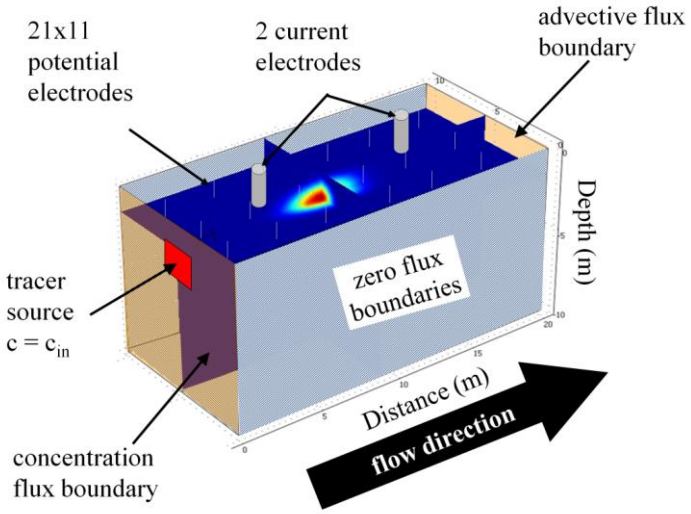

b)

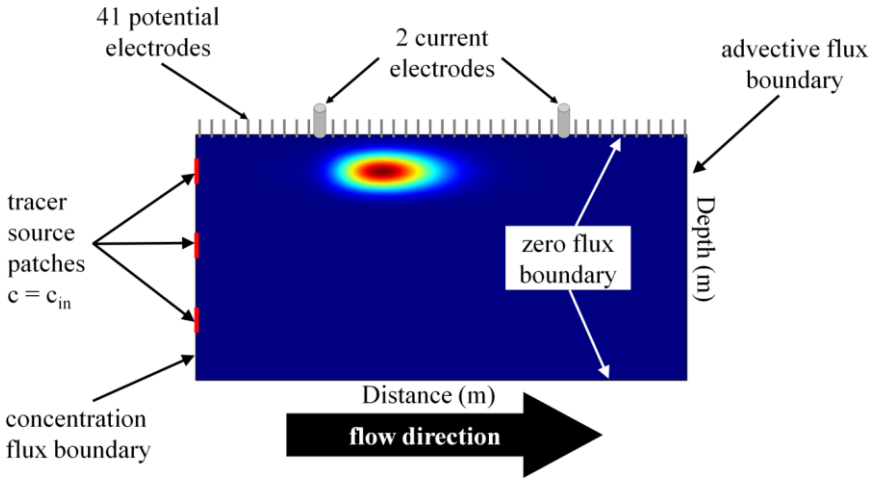

Figure 2.2: Geometry, boundary conditions, and electrode configuration for the optimization (a) and the sensitivity analysis (b).

2.4.3 Rock Physics Relationships: Archie's Law

Given the solution of the transport problem the resulting concentrations at each time step must be converted to resistivity values. Archie's law [Archie 1942] is an empirical relationship between the bulk electrical resistivity of a porous medium, ρ_{eff}, and the resistivity of the pore fluid, ρ_w. In a water saturated medium with non-conductive minerals Archie's law is

$$\rho_{eff} = aF\rho_w , \tag{2.5}$$

where the formation factor, $F = n^{-m}$, is a constant that relates the resistivity of the rock to the resistivity of the pore water. The cementation exponent m is related to the tortuosity of the medium and a is a scaling factor. The relationship between fluid resistivity and total dissolved solids concentration cited by [Lesmes and Friedman, 2005] together with a formation factor consisting of a cementation exponent of 1.3 in Archie's law are combined to define the local relationship between electrical conductivity (S/m) and solute concentration c (mg/L) is defined as

$$\rho(x, y, z, t) = 6.7 \times 10^{-3} n^{1.3} c(x, y, z, t) . \tag{2.6}$$

2.4.4 Resistivity Survey Simulations

The voltage (V) distribution in the subsurface is governed by

$$\nabla \cdot \left(\frac{1}{\rho} \nabla V \right) = \delta_{(x,y,z)} I , \tag{2.7}$$

where ρ is the resistivity and $\delta_{(x,y,z)}I$ is a point current source. Current flow in the medium is induced by fixing a voltage difference of 10V between the current electrodes located at

positions (x, y, z) = (5, 5, 0) and (15, 5, 0). All sides of the model domain were set to be electrically insulating (zero flux) boundaries. Potential electrodes are treated as poles relative to a reference electrode outside of response area. The electrodes are located at the ground surface (z = 0) and configured in a 21 x 11 grid with a spacing of 0.5 m (Figure 2.2). The data are collected continuously from the time the tracer is initially released, t_0, with a time interval of t_{int}. For the inversion and sensitivity analysis the 10 most relevant time steps (i.e. times in which the voltage changes were largest) were chosen and the models were run only for the 10 times and t_0.

2.4.5 Optimization of Hydraulic Conductivity

The coupled flow, transport and resistivity models are used to simulate sets of reference voltages, V^{ref}, for several different reference values of hydraulic conductivity (K^{ref} = 1.00 x 10^{-4}, 6.99 x 10^{-6}, and 8.12 x 10^{-3} m/s). Each set of voltage set is then used within the IDF framework (Figure 2.1) to determine if it is possible to accurately estimate the reference hydraulic conductivity from the geophysical measurements. The optimization of hydraulic conductivity is performed by minimizing the sum of squared differences between the simulated voltage response for trial values of hydraulic conductivity, i.e., $V_{i,j}(K)$, and the voltages given in the reference data set, i.e., $V_{i,j}^{ref} = V_{i,j}(K^{ref})$:

$$E(K) = \sum_{j=1}^{N_t} \sum_{i=1}^{N_e} (V_{i,j}(K) - V_{i,j}^{ref})^2 . \qquad (2.8)$$

Here N_e is the total number of potential electrodes and N_t is the total number of observation times. If the data misfit has met the stopping criteria threshold, then the "best fit" hydrologic parameter estimates are output and the simulations stop. If not, the input hydrologic parameters are updated and the sequence begins again. The optimization is performed using the SNOPT [Gill et al., 2005] algorithm from COMSOL's optimization lab toolkit [COMSOL, 2006b].

2.4.6 Sensitivity Analysis

While the optimization experiments will show whether it is possible to estimate hydraulic conductivity from resistivity data, it is important to also consider how the sensitivity of the data to this parameter changes as a function of environmental conditions. In other words, will it be possible to estimate *K* under non-optimal experimental conditions? Therefore, the second objective of this work is to determine the sensitivity of *K*-estimates in relation to changes in experimental conditions. In particular, we consider how variables that affect the sensitivity or quality of the resistivity data affect our ability to estimate *K*. The specific variables considered in this study are: (1) tracer concentration (C_{in} = 0.01, 0.05, 0.1, and 0.5 M), (2) the depth of the top tracer source zone relative to the electrodes (*tpd* = 1, 4, and 7m), and (3) the degree of background noise in the resistivity data (*bgn*), which is controlled by adding 0, 5, 10, 20% random Gaussian noise to the reference voltages. For each case, the objective function is calculated for 26 different logarithmically spaced values of *K* between 10^{-8} m/s and 1.0 m/s for the scenario where $K^{ref} = 1.0 \times 10^{-4}$ m/s. A total of 1248 simulations

are required for this analysis. To minimize computational demands, we therefore chose to perform the analysis using two-dimensional simulations taking the longitudinal cross-section of the model geometry shown in Figure 2.2. Although this geometry is not directly analogous to the three-dimensional simulations, we suggest that the general inferences made about model sensitivity are applicable to a wide range of scenarios. The results are evaluated by comparing the objective functions for the different experimental conditions.

2.5 Results

The results of the IDF *K*-optimization are displayed graphically in Figure 2.3 as a log of sum of squared voltage difference (SSVD) versus log *K* and numercially in Table 2.1 which contains the values of K^{ref} (m/s), the *K*-estimate, K_E (m/s), percent error (%), and sample rate (Hz) for Runs # 1-4. The optimizations for run # 1 and run # 2 are displayed by the green triangle and blue circle markers respectively. Both run # 1 and run # 2 achieved a unique minimum *K*-estimate, K_E, where the percent errors are 10^{-3} and 0.5 % respectively. The sample rate for each run was 2×10^{-3} Hz. The optimizations for run # 3 and run # 4 used the same reference data and thus the same K^{ref} and are displayed by the cyan square and the red diamond respectively. The run # 3 optimization failed and output the *K*-boundary value of 10^{-7} m/s. The sample rate of run # 3 was increased from 2×10^{-3} to 2×10^{-2} Hz for run # 4. The run # 4 optimization achieved a unique minimum K_E where the percent error is 6×10^{-4} %.

The results indicate that it is possible to estimate the hydraulic conductivity from the voltage data, K_E to less than 1% relative error for three values of K^{ref}. An exception is run #3 where it was not possible to estimate the hydraulic conductivity. In this case K^{ref} = 8.12x10^{-3} m/s, which is 81 times larger than the next largest value of the K^{ref} =1x10^{-4} m/s used in run #1. The reason for the estimation failure is due to under-sampling for run #3. Although a sampling rate of about 8 minutes between measurements was adequate for run #1 and #2, the higher hydraulic conductivity in run #3 causes more data to be collected when the plume is located away from the region of sensitivity for the current electrodes.

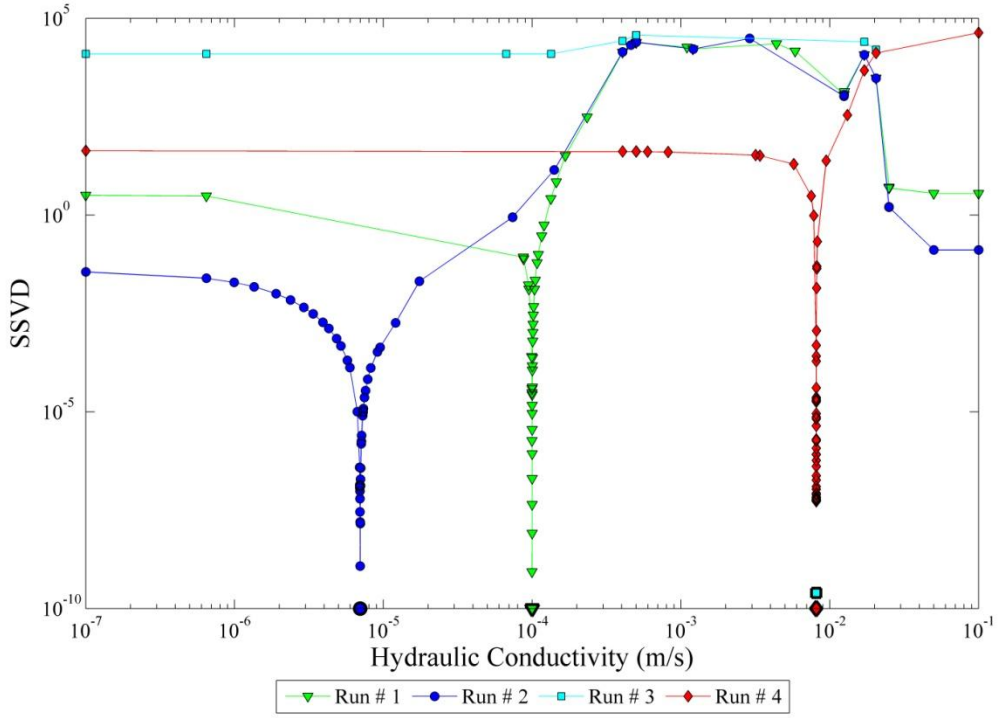

Figure 2.3: Results of the IDF *K*-optimization showing the objective function, sum of squared voltage difference (SSVD) vs. *K* for runs 1-4. The markers indicate the value of the reference *K*, K^{ref}, for each run.

Table 2.1: Reference, K^{ref}, and K-estimates, K_E (m/s), percent error (%), and sampling rate (Hz) for the four simulations run for the optimization.

Parameter	**Run #1**	**Run #2**	**Run #3**	**Run #4**
K^{ref} (m/s)	$1.00\text{x}10^{-4}$	$6.99\text{x}10^{-6}$	$8.12\text{x}10^{-3}$	$8.12\text{x}10^{-3}$
K_E (m/s)	$9.99\text{x}10^{-5}$	$6.95\text{x}10^{-6}$	$1\text{x}10^{-7}$	$8.12\text{x}10^{-3}$
Error (%)	0.0010	0.52	>1000	0.00062
Sample Rate (Hz)	$2 \text{ x } 10^{-3}$	$2 \text{ x } 10^{-3}$	$2 \text{ x } 10^{-3}$	$2 \text{ x } 10^{-2}$

The lack of sensitivity to hydraulic conductivity in this case is clearly apparent in the objective functions shown in Figure 2.3. The solution to this problem is simply to increase the sampling rate to ensure that data are collected when the plume is located near the current electrodes (run #4). Although this problem is a straightforward one, it clearly illustrates the importance of appropriate choice of sampling design for monitoring dynamic processes.

Figure 2.4 displays the sensitivity to injection concentration (C_{in}) with variable background noise (*bgn*) as a log sum of squared voltage difference (SSVD) versus log hydraulic conductivity (K). The tracer patch depth (*tpd*) is fixed at 1 m. The figure is split into four parts where a-d corresponds to increasing C_{in} with values of 0.01, 0.05, 0.1, and 0.5 M. The four lines in each subplot correspond to the level of added background noise (*bgn*) where the red triangle, blue circle, green square, and cyan diamond markers correspond to 0, 5, 10, and 20 % Gaussian noise added to the reference data respectively. Qualitatively, the figure shows that as C_{in} increases, even with an increase in *bgn*, sensitivity to K^{ref} increases. Conversely, with a low C_{in} and high *bgn* there is a loss in sensitivity to K^{ref}.

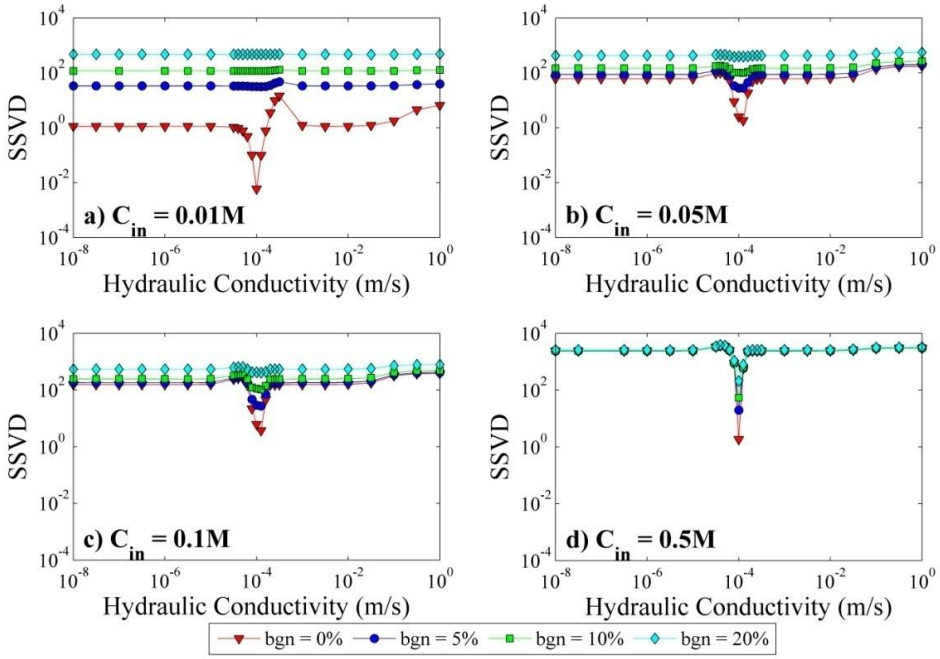

Figure 2.4: Sensitivity to injection concentration (C_{in}) with variable background noise (*bgn*) and a fixed tracer patch depth (*tpd*) = 1m displayed on a log-log plot of sum of squared voltage differences (SSVD) vs. hydraulic conducitivity.

Figure 2.5 displays the sensitivity to noise in voltages (*bgn*) with variable tracer patch depth (*tpd*) as a log sum of squared voltage difference (SSVD) versus log hydraulic conductivity (*K*). The injection concentration (C_{in}) is fixed at 0.5 M. The figure is split into four parts where a-d corresponds to increasing *bgn* with values of 0, 5, 10, and 20 % of Gaussian noise added to the reference data. The three lines in each subplot correspond to the injection depth (*tpd*) where the red triangle, blue circle, green square markers correspond to 1, 4, 7 m center depth of the 1 m high tracer patch respectively. Qualitatively, the figure shows that as *bgn* and *tpd* increases, the sensitivity to K^{ref} decreases. Conversely, with a low *bgn* and shallow *tpd* there is an increase in sensitivity to K^{ref}.

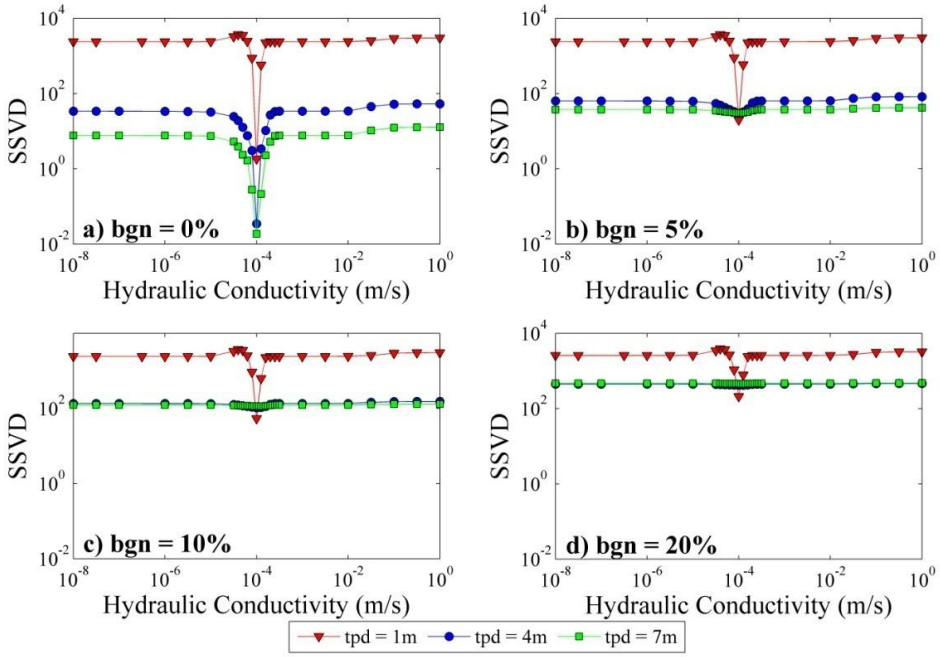

Figure 2.5: Sensitivity to noisy voltages (*bgn*) with variable tracer patch depth (*tpd*) and a fixed injection concentration (C_{in}) = 0.5M displayed on a log-log plot of sum of squared voltage differences (SSVD) vs. hydraulic conducitivity.

Figure 2.6 displays the sensitivity to tracer patch depth (*tpd*) with variable injection concentration (C_{in}) as a log sum of squared voltage difference (SSVD) versus log hydraulic conductivity (K). The background noise (*bgn*) is fixed at 0 %. The figure is split into three parts where a-c corresponds to increasing *tpd* with values of 1, 4, and 7 m. The four lines in each subplot correspond to the level of added injection concentration (C_{in}) where the red triangle, blue circle, green square, and cyan diamond markers correspond to 0.01, 0.05, 0.1, and 0.5 M respectively. Qualitatively, the figure shows that as *tpd* increases, regardless of the magnitude of C_{in}, the signal strength decreases. Conversely, with a shallower *tpd* there is an increase in signal strength. There is, for all *tpd* and C_{in} values a high sensitivity to K^{ref}.

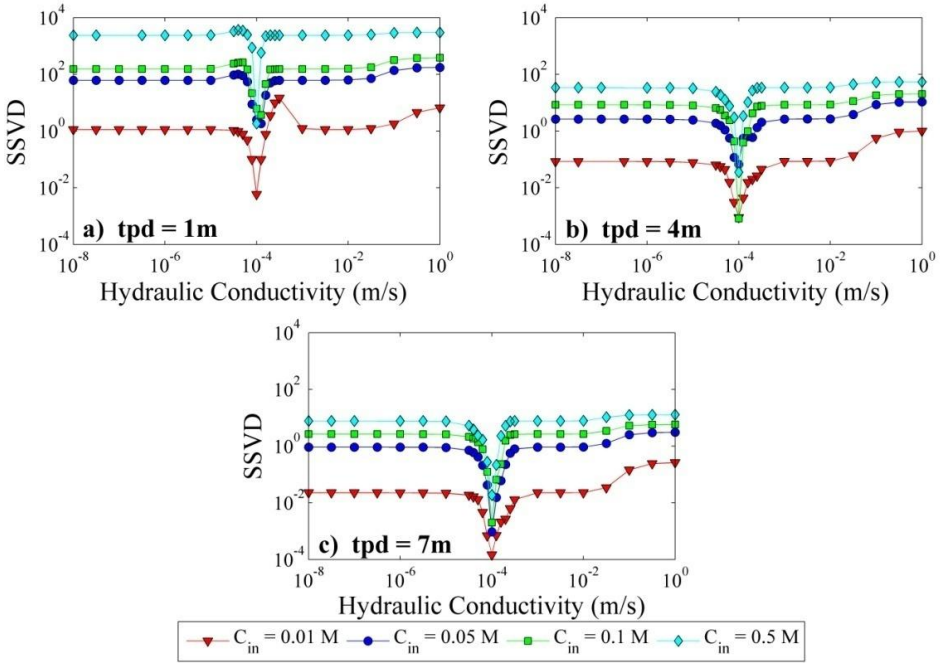

Figure 2.6: Sensitivity to tracer patch depth (*tpd*) with variable injection concentration (C_{in}) and a fixed background noise (*bgn*) = 0% displayed on a log-log plot of sum of squared voltage differences (SSVD) vs. hydraulic conductivity.

The sensitivity analysis shows that the quality of the objective functions for estimating *K* improves as the concentration of the plume is increased, the plume is located near the surface, and the degree of electrical noise is low (Figures 2.4, 2.5, and 2.6). These findings are consistent with intuition. For example, as the amount of noise in the voltage data is increased the voltage response is lost in the noise for low solute concentrations (Figure 2.4a), but clearly visible even in noisy data at high solute concentrations (Figure 2.4d). The absolute magnitude of the objective function also varies significantly for the different scenarios. This is of practical importance as the magnitude of the objective function defines the sensitivity required for a measurement instrument to detect the voltage response. Given that this study is a numerical one, however, the focus is not on the absolute magnitude of the objective function, but rather

on how well hydraulic conductivity could be constrained assuming the voltages can be measured. We are therefore interested in defining measures that describe the shape of the objective function that can be compared between the different simulation scenarios.

2.6 Discussion

Some fundamental questions that can be asked regarding the quality of the objective function include: (1) How close is K_E to K^{ref}?, (2) How identifiable is K_E?, and (3) How unique is K_E? To answer these questions, several different measures are defined. The first measure is the relative error in the estimated value of K given by

$$RE_K = \frac{\left|K_E - K^{ref}\right|}{K^{ref}}, \tag{2.9}$$

where K_E is the hydraulic conductivity value when the objective function is at a minimum and K^{ref} is the true hydraulic conductivity. The value of K_E provides an assessment of how well the hydraulic conductivity could be estimated given a certain set of environmental variables.

The second measure is the height of the objective function given by

$$H = \frac{\left|E_{\min} - \bar{E}\right|}{\bar{E}}, \tag{2.10}$$

where $\bar{E}$ and E_{min} are the mean and minimum of the objective function respectively. This measure provides a normalized value of the magnitude of the voltage error that varies between 0 and 1. A value of $H = 0$ indicates that the minimum of the objective function is equal to the background variability, and the objective function therefore contains no information to constrain hydraulic conductivity. In contrast, $H = 1$ indicates that errors

caused by data misfit are much greater than background variability, such that the objective function minimum at the optimal value of hydraulic conductivity is readily identifiable.

The third measure is the width (W) of the objective function as given by

$$W = \left| \left(0.75\bar{E} - \frac{b_r}{m_r} \right) - \left(0.75\bar{E} - \frac{b_l}{m_l} \right) \right|, \tag{2.11}$$

where b and m are the intercept and slope of the left (l) and right (r) side of the objective function. The location of $0.75\bar{E}$ is determined by estimating the slope of the objective function curve and interpolating to the position. The value $0.75\bar{E}$ provides a width equivalent to 3.28 standard deviations if the objective function were a Gaussian distribution. Since the objective functions tend to be insensitive to changes in hydraulic conductivity away from the minimum, the width provides a measure of how easily the minima could be detected; it will be difficult for a search algorithm to find the region around the global minima if the objective function width is small compared to an objective function with a large width.

The ratio of the height to width of the objective function provides a measure of the average curvature (χ) near the minimum of the objective function (Equation 2.12).

$$\chi = \frac{H}{W} \tag{2.12}$$

Curvature of the objective function, i.e., the second derivative at the minima, is an important parameter for describing the uniqueness of parameter estimates. An objective function with low curvature is indicative that the data provide a non-unique and uncertain

estimate of the parameters. In contrast, a high curvature indicates that the parameters are able to be uniquely constrained by the data.

For an example of these measures, three vastly different generic objective function curves are used. Table 2.2 contains the numerical values for E, E_{min}, K^{ref}, K_E, RE_K, W, H, and χ. Also using the generic objective function curves, Figure 2.7 illustrates the methodology for attaining the goodness of fit measures RE_K, H, W and χ where: a) the three objective function lines, b) a representation of a normal probability distribution with a width of 3.28 standard deviations corresponding to 0.75 of the height of the curve and 90% confidence, c) how H of the red curve is calculated, and d) how the normal distribution corresponds to W of the red curve. Analyzed alone, the measures W and H do not have a significant meaning, but when combined in the χ measure, they are a superb measure of the uniqueness of the solution.

Table 2.2: Generic example of goodness of fit measures.

	Measure							
Line	$\bar{E}$	E_{min}	K^{ref} (m/s)	K_E (m/s)	RE_K (%)	W (m/s)	H	χ
Red diamond	98.7	1.0	1×10^{-4}	1×10^{-4}	0	2.0×10^{-5}	0.99	5.1×10^{4}
Blue Circle	197.7	165.0	1×10^{-4}	1×10^{-4}	0	2.0×10^{-4}	0.17	830
Green Triangle	300	299.9	1×10^{-4}	9×10^{-5}	0.1	1.8×10^{-4}	3.1×10^{-4}	1.8

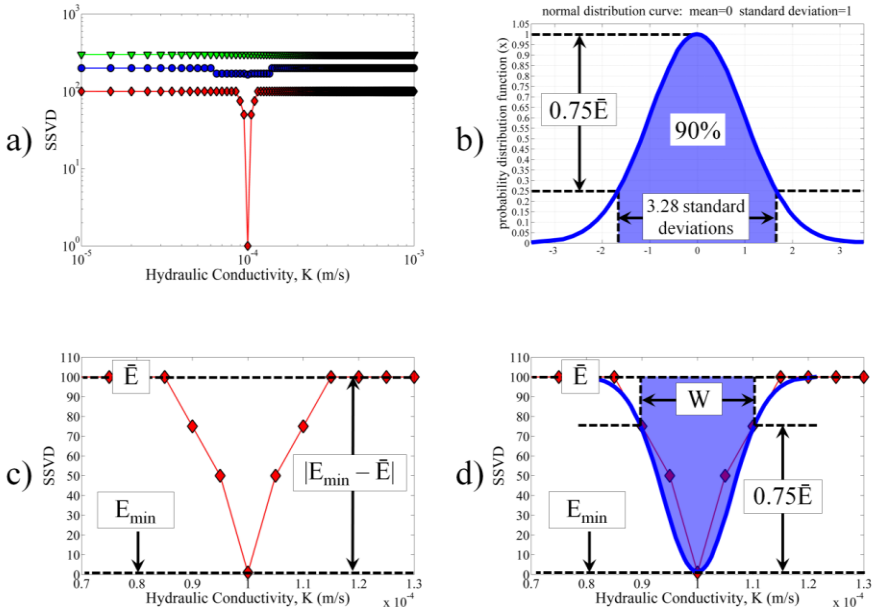

Figure 2.7: A visual example how the variables used to calculate goodness of fit measures, RE_K, H, W and χ are defined using the generic example where a) are the three curves analyzed on a log SSVD vs. a log K plot, b) is the normal probability distribution,, c) H visual description, and d) W visual description with the normal probability distribution overlaid.

The results of the goodness of fit analysis are presented in Figure 2.8 where 2.8a-d is RE_K, W, H, and χ versus C_{in} with a fixed *tpd* of 1 m and 2.8e-h is RE_K, W, H, and χ versus *tpd* with a fixed C_{in} of 0.1 M. The blue circle, red square, green triangle, and cyan diamond markers correspond to a random Gaussian noise (*bgn*) added to the reference voltages of 0, 5, 10, and 20 % respectively.

The values of RE_K show that for high concentrations, K can be successfully estimated without regard to the noise in the voltages. On the other hand, in regards to *tpd*, when the tracer is injected too close to the surface (i.e. too close to the current source) there may be the chance to get additional inaccuracies in the observations that is not directly related to the ambient noise.

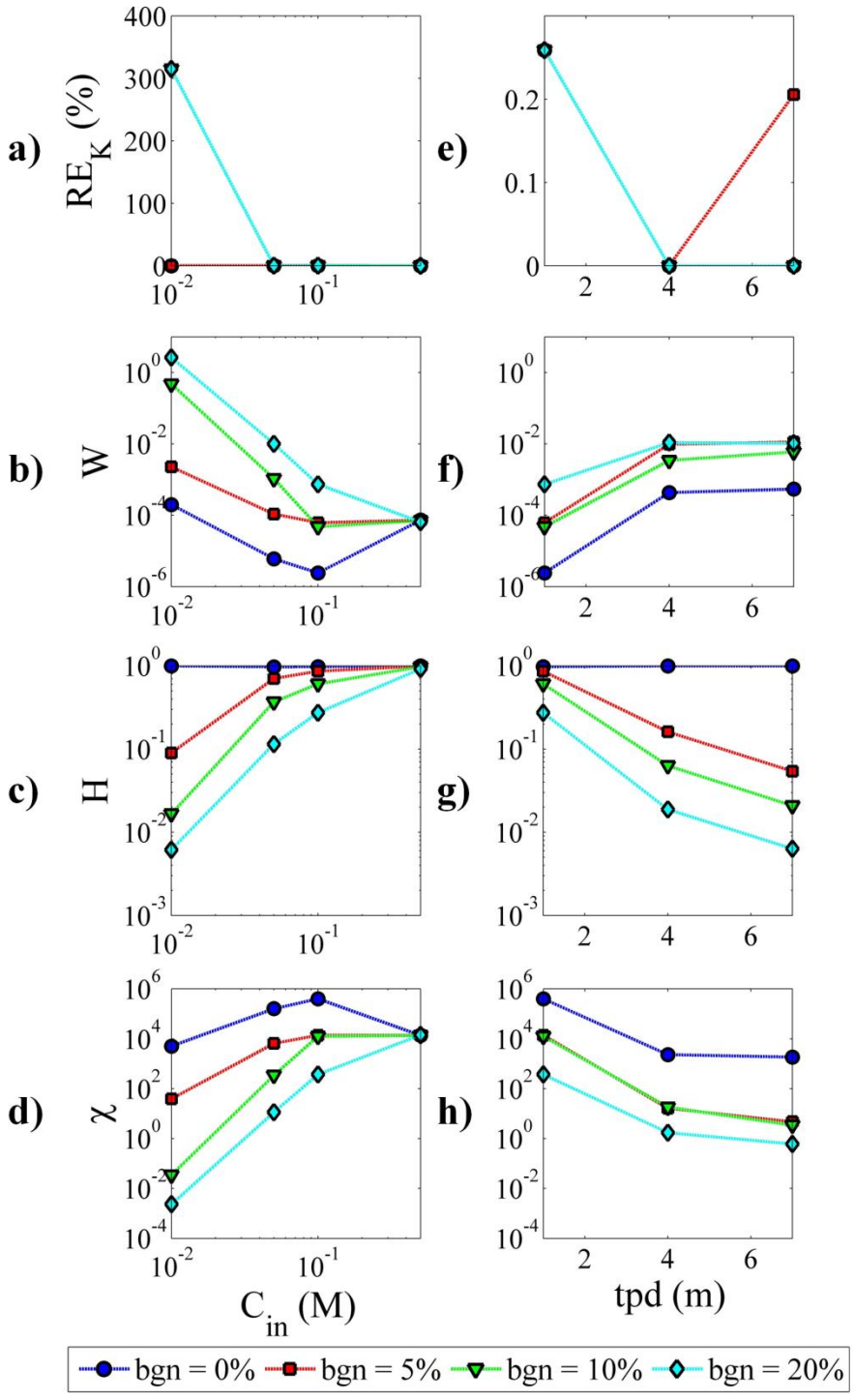

Figure 2.8: Analysis of data from the sensitivity analysis showing a) RE_K, b) H, c) W, and d) χ vs. C_{in} at a fixed *tpd* of 1m and e) RE_K, f) H, g) W, and h) χ vs. *tpd* at a fixed C_{in} of 0.1M. The lines on each plot correspond to the percent of random Gaussian noise (*bgn*) added to the reference voltages.

When varying injection concentration and depth, the value of *H* indicate that as injection concentration increases and depth decreases, the minimum of the objective function becomes more identifiable. The same trend is revealed by *W* and χ, where as injection concentration increases and depth decreases (in general), the minimum of the objective function becomes more unique. In all of the cases, with a decrease in noise in voltages, there is an increase in χ.

This analysis points towards the necessity of having additional information concerning the survey location prior to commencement of the full-scale tracer test or using prior survey results to design a better survey. Having some idea about the ideal balance between injection depth and injection concentration will yield more successful experimental results. To this end, a similar synthetic sensitivity analysis should be conducted prior to the tracer test. Consider concentration for instance: would the required minimum injection concentration be within safety limits, or would an alternative method, such as injecting pure water, need to be considered? A survey location's unique hydrologic spatial layout (i.e. the hydrologic conceptual model) and a gauge of the background noise should be ascertained and included in the analysis.

2.7 Conclusions

The most important result from the optimizations is that *K* is successfully estimated using IDF. Another important result from this set of simulations was provided in Runs 3 and 4, where the sampling rate was insufficient for the first simulation. An increase in *K*, and subsequent change in tracer velocity and dispersion, caused the *K*-

estimate to be equal to the lower search algorithm threshold. This obvious underestimate was caused by keeping the sampling rate constant, although the velocity was increased. By scaling the sampling rate to better reflect *K*, the simulation was able to capture the plume in Run #4.

This evaluation demonstrates IDF's possible value when assessing electrical data collected during an electrically conductive tracer test. In the synthetic cases evaluated, IDF is a promising tool for estimating *K* using surface voltage measurements, even though only a single current electrode pair is used. The need for rapid, time-sensitive capture of electrical data is crucial when conducting a tracer test; consequently the data must be collected quicker than most multi-current electrode surveys will allow. This shows that for a simple case, use of one current electrode pair and many potential electrodes can be sufficient for transient data collection.

Regarding the sensitivity analyses, there is generally a better estimate of *K* with lower noise, higher concentration, and a moderate injection depth. There is generally a more identifiable objective function with lower noise, higher concentration, and a shallower depth of injection. The objective function was more unique, generally, with a lower noise, higher concentration, and a shallower depth of injection.

Having some knowledge of the hydrologic conditions and relative background noise, and thus forming a good conceptual model is paramount to yielding useful results. It has been found that a similar synthetic sensitivity analysis would likely need to be run prior to the start of a survey to determine what injection depth and concentration would be optimal.

2.8 References

Archie, G. E. (1942), The electrical resistivity log as an aid in determining some reservoir characteristics, *Trans. Am. Inst. Min. Metall. Pet. Eng*., 146, pp. 54– 62.

Bear, J. (1979), *Hydraulics of groundwater*, McGraw Hill, New York, 569 p.

Binley, A., G. Cassiani, R. Middleton, P. Winship (2002), Vadoze zone flow model parameterisation using cross-borehole radar and resistivity imaging, *Journal of Hydrology*, vol. 267, no. 3-4, pp. 147-159.

Bouwer, H. (1989), The Bouwer and Rice slug test--an update, *Ground Water*, 27, 304-309.

Bouwer, H. and R.C. Rice (1976), A slug test method for determining hydraulic conductivity of unconfined aquifers with completely or partially penetrating wells, *Water Resources Research*, vol. 12, no. 3, pp. 423-428.

Comsol Multiphysics 3.3a: User's Guide (2006), www.comsol.com.

Comsol Multiphysics 3.3a: Optimization Lab User's Guide, Version 1.0 (2006), www.comsol.com.

Daily, W., A. Ramirez, D. LaBrecque, J. Nitao (1992), Electrical resistivity tomography of vadoze water movement, *Water Resources Research*, vol. 28, no. 5, pp. 1429-1442.

Darcy, H. (1856), *Les fontaines publiques de la ville de Dijon*. Paris: Victor Dalmont.

Fetter, C.W. (2001), *Applied hydrogeology*. Prentice Hall, Upper Saddle River, N.J., 4th Ed., 598p.

Feehley, C. H., C. Zheng, F. J. Molz (2000), A dual-domain mass transfer approach for modeling solute transport in heterogeneous aquifers, *Water Resources Research*, vol. 36, no. 9, pp. 2501-2515.

Fitts, C. R. (1996), Uncertainty in deterministic groundwater transport models due to the assumption of macrodispersive mixing: evidence from the Cape Cod (Massachusetts, U. S. A.) and Borden (Ontario, Canada) tracer tests, *Journal of Contaminant Hydrology*, 23, 69-84.

Gill, P. E., W. Murray, M. A. Saunders (2005), User's guide for SNOPT 7: A Fortran package for large-scale nonlinear programming, *Numerical Analysis Report NA 05-1*, Department of Mathematics, University of California, San Diego, La Jolla, CA.

Hinnell, A. C. , T. P. A. Ferre, J. A. Vrugt, J. A. Huisman, S. Moysey, J. Rings, M. B. Kowalsky (2010), Improved extraction of hydrologic information from geophysical data through coupled hydrogeophysical inversion, *Water Resources Research*, vol. 46, W00D40.

Huisman, J. A, J. Rings, J.A. Vrugt, J. Sorg, H. Vereecken (2010), Hydraulic properties of a model dike from coupled Bayesian and multi-criteria hydrogeophysical inversion, *Journal of Hydrology*, vol. 380, pp. 62–73.

Hvorslev, M. J. (1951), Time lag and soil permeability in ground-water observations, *Bull. No. 36, Waterways Exper. Sta. Corps of Engrs*, U.S. Army, Vicksburg, Mississippi, pp. 1-50.

Jacob, C. E. (1940), On the flow of water in an elastic artesian aquifer, *Transactions, American Geophysical Union*, 21, pp. 574-586.

Kemna, A., J. Vanderborght, B. Kulessa, and H. Vereeken (2002), Imaging and characterisation of subsurface solute transport using electrical resistivity tomography (ERT) and equivalent transport models, *Journal of Hydrology*, vol. 267, no. 3-4, pp. 125-146.

Kowalsky, M. B., S. Finsterle, J. Peterson, S. Hubbard, Y. Rubin, E. Majer, A. Ward, G. Gee (2004), Estimation of field-scale soil hydraulic and dielectric parameters through joint inversion of GPR and hydrological data, *Water Resources Research*, vol. 41, W11425.

Kowalsky, M. B., S. Finsterle, Y. Rubin (2005), Estimating flow parameter distributions using ground-penetrating radar and hydrological measurements during transient flow in the vadose zone, *Advances in Water Resources*, vol. 27, pp. 583–599.

Lambot, S., E. C. Slob, M. Vanclooster, H. Vereecken (2006), Closed loop GPR data inversion for soil hydraulic and electric property determination, *Geophysical Research Letters*, vol. 33, no. 21, L21405.

Lesmes, D. P., S. P. Friedman (2005), Relationships between the electrical and hydrogeological properties of rocks and soils, In: Rubin, Y, S. S. Hubbard (eds) *Hydrogeophysics, Chapter 4*, Springer, Dordrecht, The Netherlands, pp 87–128.

Looms, M. C., A. Binley, K. H. Jensen, L. Nielsen, T. M. Hansen (2008), Identifying unsaturated hydraulic parameters using an integrated data fusion approach on cross-borehole geophysical data, *Vadoze Zone Journal*, 7(1), 238-248.

Molz, F. J., J. G. Melville, O. Guven, R. D. Crocker, K. T. Matteson (1985), Design and performance of single-well tracer tests at the Mobile site, *Water Resources Research*, vol. 21, no. 10, pp. 1497-1502.

Moysey S., R. J. Knight, K. Singha (2006), Relating geophysical and hydrologic properties using field-scale rock physics, *CMWR XVI -- Computational Methods in Water Resources*, Copenhagen, Denmark, 8p.

Moysey, S., K. Singha, R. Knight (2005), A framework for inferring field-scale rock physics relationships through numerical simulation, *Geophysical Research Letters*, 32, L08304.

Rucker, D. F., T. P. A. Ferre (2004), Parameter estimation for soil hydraulic properties using zero-offset borehole radar: Analytical method, *Soil Science Society of America Journal*, vol. 68, pp. 1560-1567.

Singha, K., S. M. Gorelick (2006), Effects of spatially variable resolution on field-scale estimates of tracer concentration from electrical inversions using Archie's law, *Geophysics*, vol. 71, no. 3, pp. G83-G91.

Singha, K., S. M. Gorelick (2005), Saline tracer visualized with three-dimensional electrical resistivity tomography: Field-scale spatial moment analysis, *Water Resources Research*, vol. 41, W05023.

Singha, K., S. Moysey (2005), Accounting for spatially variable resolution in electrical resistivity tomography through field-scale rock-physics relations, *Geophysics*, vol. 71, no. 4, pp. A25-A28.

Slater L., A. M. Binley, W. Daily, R. Johnson (2000), Cross-hole electrical imaging of a controlled saline tracer injection, *Journal of Applied Geophysics*, vol. 44, no. 2-3, pp. 85-102.

Sudicky, E. A. (1986), A natural gradient experiment on solute transport in a sand aquifer: spatial variability of hydraulic conductivity and its role in the dispersion process, *Water Resources Research*, 22(13), 2069-2082.

Theis, Charles V. (1935), The lowering of the piezometer surface and the rate and discharge of a well using ground-water storage, *Transactions, American Geophysical Union*, 16, 519-524.

CHAPTER 3

EVALUATING THE CONSEQUENCES OF DATA SENSITIVITY FOR CONSTRAINING AQUIFER TRANSPORT MODELS WITH ELECTRICAL RESISTIVITY DATA IN A COUPLED INVERSION FRAMEWORK[1]

3.1 Abstract

Integrated data fusion (IDF) or coupled inversion (CI) is gaining wider use in terms of hydrogeophysical model calibration and optimization. IDF is being used in this research as an approach to geophysical data inversion that couples mathematical models of groundwater flow, solute transport, and electrical resistivity for the direct estimation of hydraulic conductivity, porosity, and dispersivity from transient resistivity data collected during a tracer test. The purpose of this study is to look at three primary hydrologic parameters that characterize contaminant transport (hydraulic conductivity, porosity, and dispersivity) with regard to model sensitivity to changes in these parameters. For this purpose, an analytical solution for flow and a point release of solute are coupled with a numerical simulation for electrical resistivity and used to generate synthetic observational data. The observational data are then compared to model data generated using the same numerical design with variations in the transport parameters to determine data sensitivity to the parameters. The simulations indicate that resistivity data can be used within the IDF framework to constrain hydraulic conductivity and porosity quite well using Darcy's Law and Archie's Law, but there still remains some non-uniqueness in dispersivity

[1] This chapter has been submitted for publication to *Journal of Hydrology*.

values related to size, shape, and location of the plume and the relation to the resistivity data.

3.2 Introduction

Electrical resistivity surveys are an increasingly important method for imaging subsurface flow and transport processes. There is now a substantial body of literature illustrating the use of high-resolution imaging methods in the lab to observe changes in resistivity related to solute movement through soil cores [Binley et al., 1996; Olsen et al., 1999; Koestel et al., 2008 and 2009]. Likewise, there are a growing number of examples where resistivity imaging by borehole tomography has been used to monitor solute migration in the field [Slater et al., 2000; Singha and Gorelick, 2005 and 2006]. There are fewer examples, however, where surface-based resistivity surveys have been used to monitor subsurface transport processes [Slater and Sandberg, 2000; Uhlenbrook et al., 2008]. This is despite the fact that compared to borehole surveys, surface-based imaging is easier to deploy and can be used to investigate much larger areas than borehole surveys. Surface-based resistivity surveying could therefore provide a cost-effective means of obtaining critical information for calibrating flow and transport models.

Given that traditional resistivity imaging techniques are well established [Daily et al., 1992; Slater et al., 2000; Binley et al., 2002; Kemna et al., 2002], the most direct way to constrain transport models with resistivity data is to employ sequential data integration. In this approach, an imaging experiment is performed to map the resistivity distribution in the subsurface at one or more instances. A rock physics relationship is

then used to locally convert the estimated resistivity images to concentration maps. Finally, these concentrations can be applied as a traditional constraint in the calibration of a flow and transport model along with direct measurements of concentration and other supporting hydrologic data. The estimation of solute concentrations from a resistivity image is a key challenge in this framework. Relationships between resistivity and concentration are typically calibrated using measurements made on well-defined sample volumes, e.g., using experiments on core samples in the lab. It is also usually assumed that this relationship should follow a specific parametric form, e.g., Archie's law [Archie, 1942]. Relationships derived in this way may not, however, be valid for interpreting field-scale data. Moysey et al. [2005] and Day-Lewis et al. [2005] used numerical simulations to show that the mathematical regularization needed to stabilize the resistivity inverse problem introduces artifacts that locally change the relationship between resistivity and concentration at the field scale. In a borehole tomography experiment designed to monitor a field-scale tracer test, Singha and Gorelick [2006] found that Archie's law failed to produce concentration estimates from the resistivity images that preserved the mass of the solute unless "unrealistic" parameter values were used.

To overcome this problem, several approaches have been suggested to capture the relationship between resistivity and concentration at the field scale. Moysey et al. [2005] proposed the use of numerical analogs to quantify how resistivity imaging filters the subsurface, and then they accounted for this filtering to develop spatially variable field-scale rock physics relationships. Singha and Moysey [2006] demonstrated that the

approach could be used to improve estimates of concentration obtained from resistivity surveys. Linde et al. [2006] assume the form of Archie's law to be valid at the field scale, but estimate equivalent field-scale parameters in the relationship as part of the resistivity inversion. Koestel et al. [2009] used the transient changes observed in each pixel of a resistivity image to calibrate transport parameters. Their approach suggests that information embedded within a transient geophysical signal, such as the timing of the response, also contains information about transport processes. Therefore, alternatives to sequential data integration must also exist that avoid the geophysical imaging step and the need for field-scale rock physics relationships. Specifically, it may be possible to use the sensitivity of resistivity measurements to changes in hydrologic state to directly infer information about hydrologic processes.

This problem has received increasing attention over the last few years as coupled inversion (also known as integrated [Moysey et al., 2006] or closed-loop [Lambot, et al., 2006] inversion) and has been used to directly calibrate hydrologic process models using geophysical measurements [Rucker and Ferre, 2004; Kowalsky et al., 2004 and 2005; Lambot, et al., 2006; Looms et al., 2008; Hinnell et al., 2010; Huisman et al., 2010]. The overview of the coupled inversion procedure in Figure 3.1 illustrates that a rock physics relationship is still needed to link the hydrologic and geophysical state variables, i.e., resistivity and concentration, in order to couple the hydrologic and geophysical forward models. Moysey et al. [2006] argue, however, that the well defined support volume of grid cells in forward models overcomes the need for the field-scale rock physics methods invented for sequential data integration.

Another key advantage of coupled inversion is that the spatial and temporal evolution of subsurface resistivity is implicitly controlled by the hydrologic forward model (Figure 3.1), whereas it must be estimated in sequential inversion. As a result, far fewer parameters need to be estimated from a fixed set of geophysical observations for coupled versus sequential inversion, making the coupled approach inherently better posed as an inverse problem. In a direct comparison of sequential and coupled inversion, Hinnell et al. [2010] showed that the implicit physics-based constraint of the hydrologic forward model allowed the coupled inversion to produce both lower hydrologic parameter and prediction uncertainties. An important implication is that less data, e.g., smaller monitoring networks and fewer sampling times, may be required to constrain a flow and transport model using the coupled approach.

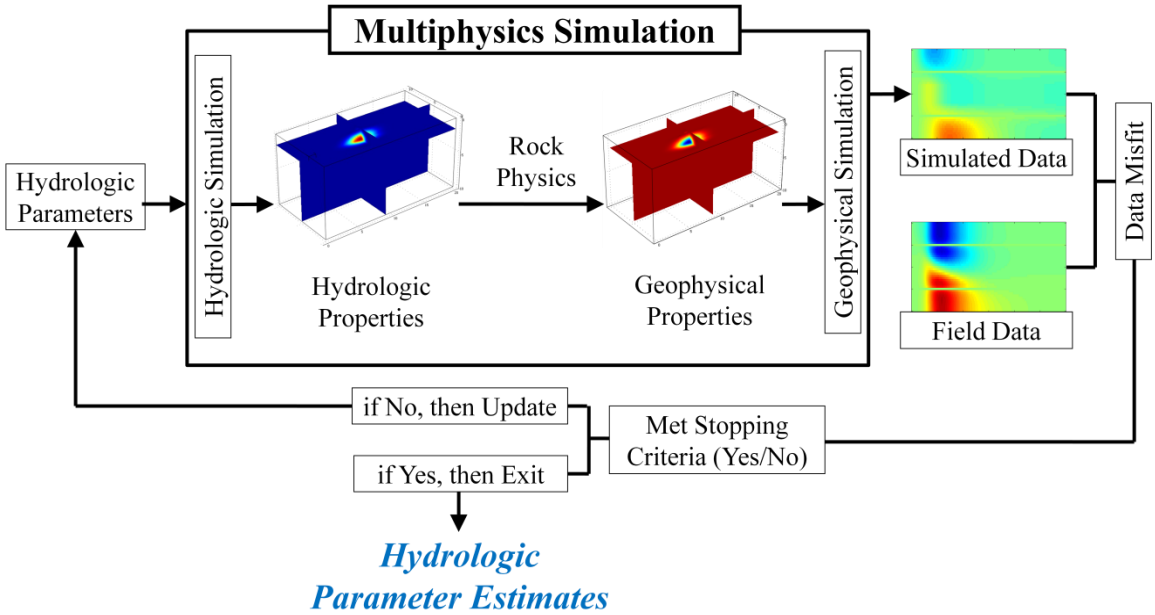

Figure 3.1: Flow schematic describing the integrated data fusion (IDF) workflow. The hydrologic and geophysical simulations, coupled by rock physics relationships, comprise the multiphysics simulation. Hydrologic parameters are the input and simulated geophysical data are output of the multiphysics simulation. The simulated geophysical data and field data are then used to compute the model data misfit. If a maximum misfit threshold condition is met, the hydrologic parameter estimates are output.

Despite the clear advantages that coupled inversion brings to hydrogeophysical estimation, there are still many unanswered questions regarding the value of the technique. In this paper, numerical simulations are used to explore the underlying value of surface-based resistivity measurements for calibrating aquifer flow and transport models in a coupled inversion framework. The long-term objective is to constrain heterogeneous flow systems using resistivity monitoring networks as illustrated by Moysey et al. [2007]. However, before that problem can be effectively addressed, it is important to understand the information content of resistivity data for simple systems. Therefore, it must be evaluated whether data generated by a single current electrode pair can uniquely constrain the parameters controlling solute transport in a homogeneous medium. Despite the apparent simplicity of this scenario, it is asserted that such studies are necessary for improving our basic understanding of coupled inversion in hydrogeophysics; a lack of data sensitivity in this simple scenario would indicate a fundamental limitation of surface-based resistivity for estimating aquifer transport parameters that would also affect estimation in heterogeneous systems. Furthermore, limiting the focus to a single pair of current electrodes facilitates the interpretation of the results and provides fundamental insights that can be generalized for designing survey arrays for more complicated transport problems.

3.3 Methods

3.3.1 Model Overview

The objective of this study is to evaluate the sensitivity of aquifer flow and transport parameters to electrical resistivity data. To this end, an investigation of the problem illustrated in Figure 3.2 is conducted using a dipole-pole survey geometry. A single pair of electrodes is used to inject current into the subsurface while an array of potential electrodes on the ground surface monitors voltage changes as the subsurface electrical conductivity, σ, varies through time and space in response to the migrating solute plume. The data in this problem are therefore $V_i(t)$, i.e., the voltage measured at potential electrode i relative to ground potential ($V = 0$) at observation time t. The voltages are found by solving the equation

$$\nabla \cdot \sigma \nabla V = 0, \tag{3.1}$$

using the finite element modeling software COMSOL Multiphysics [COMSOL, 2008], subject to zero current flux conditions at the boundaries of the simulation domain. Current flow within the subsurface is induced by setting the current electrodes to a fixed reference voltage throughout the simulations.

The conceptual model used for transport in the simulations is an instantaneous release from a point source in a geologically homogeneous medium with uniform flow. The analytical solution to the advection-dispersion equation in an infinite medium is well known for this scenario and given by Lenda and Zuber [1970] as:

$$c(x,y,z,t) = \frac{M}{8n\ \pi t^{\frac{3}{2}}\sqrt{D_x D_y D_z}} \exp\left(-\frac{x - vt^{\ 2}}{4D_x t} - \frac{y^2}{4D_y t} - \frac{z^2}{4D_z t} \right), \tag{3.2}$$

where x, y, and z are position relative to the location of the solute point source; t is time since the instantaneous release of the solute; M is the total mass of solute input at $t = 0$; n is the aquifer porosity; and, D_x, D_y, and D_z are the longitudinal, transverse horizontal, and transverse vertical dispersion coefficients for the aquifer, respectively. The dispersion coefficients are related to dispersivities for this one-dimensional flow by $D_k = \alpha_k v$. Following Freeze and Cherry [1979] and Gelhar et al. [1992], it is assumed that that $D_y \cong 0.1 D_x$ and $D_z \cong 0.01 D_x$ in the simulations, such that only a single dispersivity value controls the behavior of the plume. The uniform, one-dimensional particle velocity in this problem, v, is specified by the aquifer hydraulic conductivity, K, and hydraulic gradient, dh/dx, using Darcy's law [Darcy, 1856]:

$$v = -\frac{K}{n}\frac{dh}{dx}. \tag{3.3}$$

Given the analytical solution for concentration in Equation 3.2, the bulk electrical conductivity at any point in space and time is specified using Archie's law. The relationship between fluid conductivity and total dissolved solids concentration cited by Lesmes and Friedman [2005] is used together with a formation factor consisting of a cementation exponent of 1.3 in Archie's law to define the local relationship between electrical conductivity σ (S/m) and solute concentration c (mg/L) as

$$\sigma(x, y, z, t) = 1.5 \times 10^{-4} n^{1.3} c(x, y, z, t). \tag{3.4}$$

For all of the simulations, it was assumed that the aquifer contains a homogeneous background concentration of 146 mg/L, representing groundwater solutes present prior to the tracer experiment. We note that the choices of Archie's law parameters and

background concentration are not general and recognize that they may affect the specific results of this study, e.g., by affecting the magnitude of the electrical conductivities used in the simulations. It is not believed, however, that the choice will significantly impact the general inferences or conclusions made from our results.

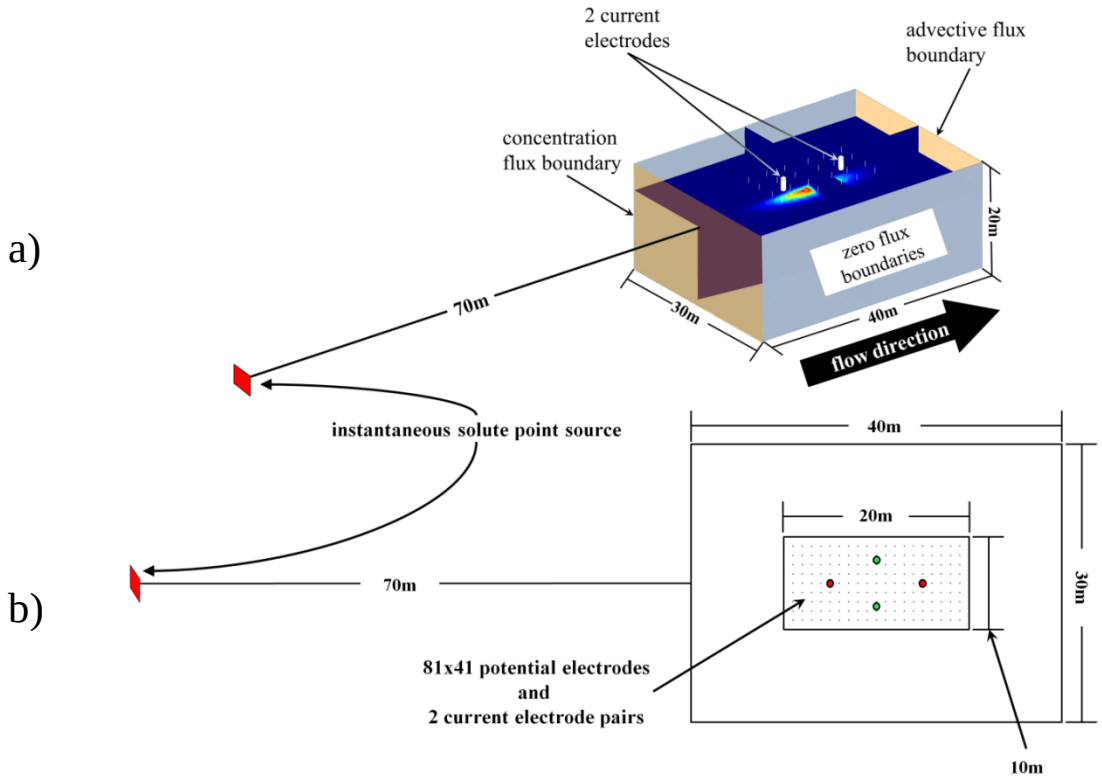

Figure 3.2: Three-dimensional geometry (a) showing geometry, flow and transport module boundary conditions, and electrode configuration and two-dimensional, plan view (b) schematic showing resistivity module geometry and electrode positions. The current pair in-line with flow is shown in red and the current pair perpendicular to flow is shown in green. Note that the potential electrode array shown is 21x11, where the actual array consists of 81x41 potential electrodes.

The source of the solute plume is placed upstream of the current electrodes to allow the plume to grow by dispersion before it reaches the region where the electrodes are located. Given that the plume does not impact current flow when it is far from the

electrodes, the resistivity simulations are only performed over the 40m (length) x 30m (width) x 20m (depth) domain shown in Figure 2. The dimensions of this region and the size of the elements within it were selected to provide a computationally feasible problem while avoiding numerical and boundary effects on current flow and minimizing mass losses from the sides of the domain for most values of dispersivity considered in this study (i.e., about 10% of the initial solute mass is lost from the simulation domain when longitudinal dispersivity is greater than 0.5m). The numerical accuracy of the resistivity simulations was checked by matching the theoretical geometric factor for a Wenner array to that calculated with the model using a homogeneous background resistivity. The simulation region is laterally centered on the current electrodes, which are located at the top surface of the domain. Two different current electrode geometries were tested to provide additional information useful for understanding measurement sensitivity. In the first case, the current electrodes are located 95m and 105m downstream of the point source along an axis parallel to the direction of flow. In the second case, the current electrodes are rotated to be perpendicular to the flow direction such that they are both 100m downstream from the point source and centered on the longitudinal axis of the model with a reduced separation of 5m due to the smaller model dimension in this direction. When the plume is outside of the simulation region, the voltage distribution is assumed to be equal to the values calculated for the background concentration. In this synthetic evaluation the vadoze zone is not incorporated.

3.3.2 Evaluation of Parameter Sensitivity

Given the model description above, there are three parameters (hydraulic conductivity - K, porosity - n, and longitudinal dispersivity - α_x) that control the behavior of the plume and, therefore, the spatial and temporal patterns of the observed voltage responses, i.e., $V_{i,j}(K, n, \alpha_x)$ where the indices i and j refer to the measurement electrode and observation time, respectively. Figure 3.3 shows the evolution of voltage at the ground surface in response to a migrating plume for the specific set of reference parameters: K^{ref} =1x10^{-4}m/s, n^{ref} = 0.3 and α_x^{ref} = 0.1m. Figure 3.3a is the sum of squared voltage differences (SSVD) vs. time and displays the times chosen, t_1 to t_5, where t = are 66, 70, 75, 80, and 85 hours respectively. Figure 3.3b is the measured surface voltage differences relative to the voltage at t_0 in the left column and the plume location in the right column. This figure visually represents how the electric potential changes relative to the location of the plume, where the maximum response at t_3 is the measure used within the objective function to determine the sensitivity of the system to the changes in measured voltage. The maximum response time directly corresponds to the time where the plume center of mass is exactly centered within the resistivity domain. It is clear from this image that the plume qualitatively affects the voltage response. It is not clear from these images, however, whether the voltage data could be used to uniquely constrain the flow and transport parameters.

To address this problem, we evaluate the degree to which the reference voltage response (Figure 3.3) changes as the transport parameters K, n, α_x are varied. To quantify this change we use the mean square of differences (i.e., MSD) between the reference

voltages, i.e., $V_{i,j}^{ref} = V_{i,j}(K^{ref}, n^{ref}, \alpha_x^{ref})$, and the voltage response calculated for an arbitrary set of test hydrologic parameters, $V_{i,j}(K, n, \alpha_x)$:

$$E(K,n,\alpha_x) = \frac{1}{N_t N_e} \sum_{j=1}^{N_t} \sum_{i=1}^{N_e} (V_{i,j}(K,n,\alpha_x) - V_{i,j}^{ref})^2 . \quad (3.5)$$

Here N_e is the total number of potential electrodes and N_t is the total number of observation times. In this example, we used the 3321 potential electrodes arranged in the 81x41 grid shown in Figure 3.2. A total of 10 observations times are used. These observation times were selected based on when the plume is located within the simulation domain for the reference case, thereby yielding a significant voltage response. The MSD is equivalent to the mean squared error (MSE) that would typically be calculated in a resistivity inverse problem by replacing the reference voltages with experimental observations. The slight distinction is made here to reemphasize that issues related specifically to field measurements (e.g., measurement noise) are not considered.

a)

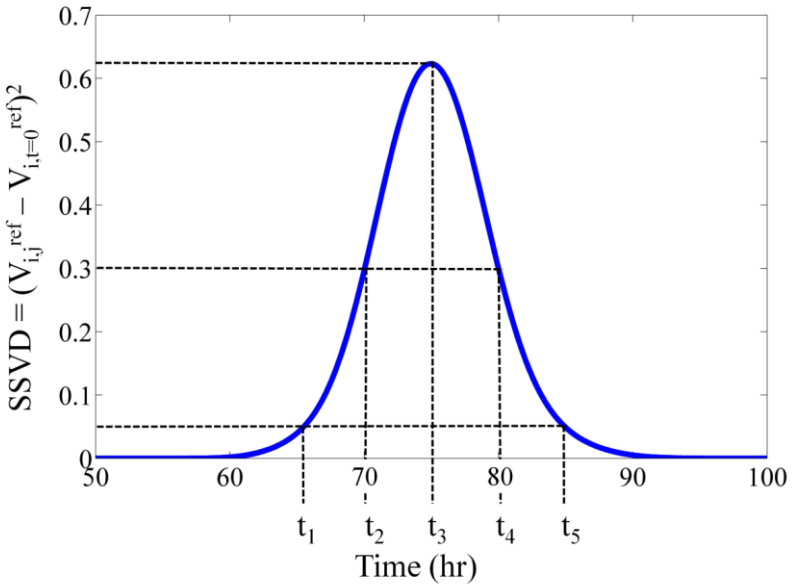

b)

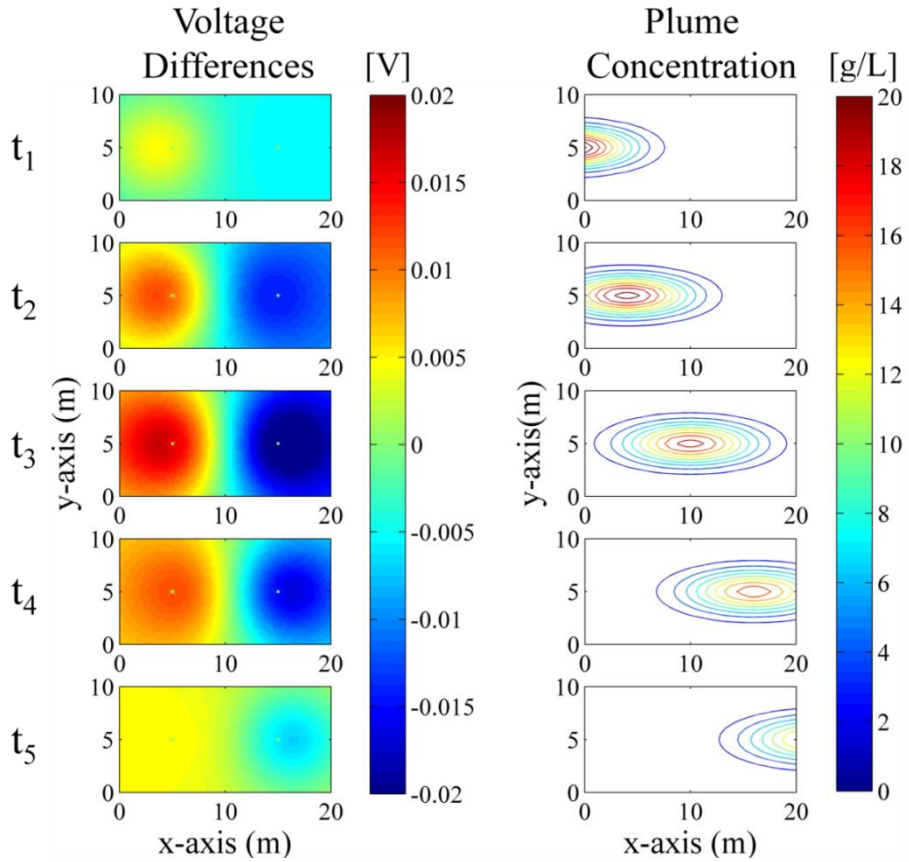

Figure 3.3: Upper plot (a) is the sum of squared voltage differences (SSVD) vs. time for the reference case (using K^{ref}, n^{ref}, α_x^{ref}) and indicates how times $t_1 - t_5$ were selected. Lower plot (b) is a comparison of voltage differences ($V_{t0} - V_t$) with plume location and concentration for each of the times in the upper plot. Times t_1 to t_5 are 66, 70, 75, 80, and 85 hours.

3.4 Results

The relative change in response at the potential electrodes for different values of the transport parameters K, n, and α_x is given in Figure 3.4 as the root of the mean squared difference in voltage (RMSD) normalized by its maximum value, i.e., $\sqrt{E} \,/\, max(\sqrt{E})$. Figure 3.4a/b) variable K and n and fixed $\alpha = \alpha^{ref}$, 3.4c/d) variable K and α and fixed $n = n^{ref}$, and Figure 3.4e/f) variable n and α and fixed $K = K^{ref}$. The

parallel and perpendicular electrode geometries correspond to Figure 3.4a/c/e and Figure 3.4b/d/f respectively. The black X in each subplot corresponds to the location in parameter space where the reference parameter pair is located. The color scale for all subplots represents the ratio $\sqrt{E} / max(\sqrt{E})$, where the white, or $\sqrt{E} / max(\sqrt{E}) = 0$, corresponds to a data misfit of zero in comparison to the reference case and black, or $\sqrt{E} / max(\sqrt{E}) = 1$, corresponds to the maximum data error. This figure is corollary to an analysis in three dimensional parameter space where each subplot (Figure 3.4a/c/e or Figure 3.4b/d/f) corresponds to a two dimensional slice in that parameter space at the location of the fixed reference parameter. The pixels in every plot correspond to a single model run.

Although the absolute RMSD is only 14mV when the electrodes are parallel to the flow and 4mV when the current electrodes are perpendicular to the flow, the difference between the two geometries causing less of the tracer to be electrically sampled (i.e. the depth of penetration of the perpendicular geometry is approximately 0.5 times that of the parallel geometry), the voltage changes at individual electrodes can be appreciably larger. For example, at the potential electrodes located at (x, y) = (16.25m, 5m), the change is 22.5mV when the electrodes are parallel to flow. When the potential electrodes are located at(x, y) = (10m, 0.75m) the change is 8.6mV when the electrodes are perpendicular to flow. Both of the previous examples of voltage changes occur when the tracer is not located within the resistivity module geometry.

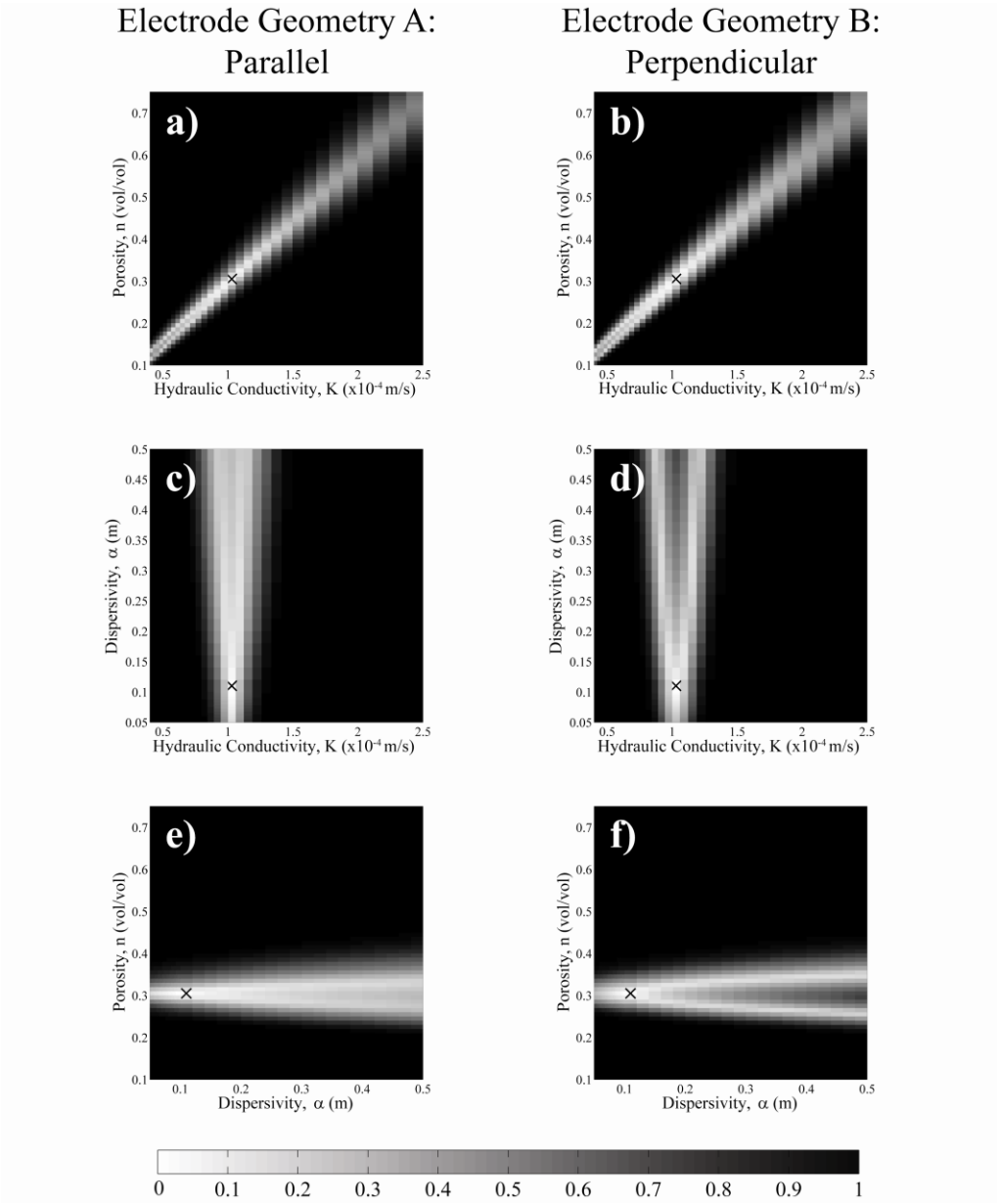

Figure 3.4: Results of the objective function sensitivity analysis with a/b) variable K and n and fixed $\alpha = \alpha^{ref}$, c/d) variable K and α and fixed $n = n^{ref}$, and e/f) variable n and α and fixed $K = K^{ref}$. The parallel and perpendicular electrode geometries correspond to a/c/e and b/d/f respectively. The black 'X' in each figure represents the location of the reference parameter pair. The color scale represents the ratio $\sqrt{E} \,/\, max(\sqrt{E})$.

Given that the simulations contained no measurement error, a unique minimum in the difference between the reference and test voltages occurs when the parameters K, n,

and α_x are equal to their reference values. This suggests that, in principle, surface-based resistivity monitoring could be used to identify aquifer flow and transport parameters. In practice, however, even when the data contain a detectable signal, noise may mask the minima leaving only the broader trends in an objective function. Successful optimization of the flow and transport parameters from field data will therefore depend on additional factors not included in this study that affect data quality, such as: the applied power and resulting signal to noise ratio of the data, the depth of the aquifer from the surface, the solute concentrations in the plume, and the background resistivity of the geologic materials. Therefore, rather than focusing on the absolute magnitude of the calculated RMSD, an emphasis is placed on understanding the patterns in Figure 3.4 that would likely be observed under higher noise levels.

For most values of K, n, and α_x the RMSD is high and the data show no sensitivity to the parameters. This is due to the fact that many combinations of the transport parameters cause the plume to be located far from the electrodes at the fixed observation times used in the synthetic experiment. For example, the plume center of mass will be located 100m downstream from the source, i.e., exactly between the current electrodes, after 83.3hrs for a simulation using the reference transport parameters. However, if the hydraulic conductivity is reduced by a factor of 1/2 while keeping the porosity and dispersivity fixed, the plume center of mass travels only 50m after 83.3hrs and practically the entire plume mass is located outside of the simulation domain. Therefore, the high RMSD value for this particular combination of parameters, like most of those in Figure 3.4, represents the difference between the reference voltages simulated

when the plume is near the electrodes versus the voltages obtained for the background material with no plume present. It is also clear, however, that there are some combinations of the flow and transport parameters that produce a voltage response that is electrically similar to the reference case, resulting in trends of low RMSD in Figure 3.4. These tradeoffs are important because they indicate inherent non-uniqueness that would confound the optimization of the transport parameters even under near ideal data acquisition conditions.

A tradeoff between hydraulic conductivity and porosity is clearly seen in Figures 3.4a and 3.4b. This non-uniqueness occurs because the ratio K/n controls the velocity of the solute plume in Equation 3.3. Therefore, any values of K and n that yield the same K/n ratio as the reference case will also produce a plume identical to the reference case, given that the dispersivity is fixed to its reference value. Changes in the K/n ratio, however, cause the plume to shift position relative to the reference case at any given observation time, thereby producing a large relative voltage difference. Notably, even when the K/n ratio is fixed to the reference value, the voltage RMSD increases as K and n are varied - this is despite the fact that the concentration distribution for the plume remains identical to the reference case. The voltage differences in this case result from the dependence of bulk resistivity on porosity in Archie's Law (Equation 3.4), which allows identical concentration profiles to produce different resistivity distributions. We note, however, that the magnitudes of the voltage changes resulting from this dependence are not as large as those caused by repositioning the plume. The patterns of voltage RMSD are similar regardless of whether the current electrodes are placed parallel or

perpendicular to the direction of transport (Figure 3.4a vs. 3.4b). Overall, the implication is that the K/n ratio is well constrained by surface resistivity data because this ratio controls the arrival of the plume in the zone of electrode sensitivity, resulting in significant changes in resistivity. In contrast, constraining the individual values of K and n depends on more subtle changes in resistivity and requires knowledge of the transform between concentration and bulk resistivity.

Figures 3.4c-d and 3.4e-f respectively show the interactions of dispersivity versus hydraulic conductivity and dispersivity versus porosity for affecting the voltage RMSD. Low values of RMSD occur over a small range of hydraulic conductivity values in Figures 3.4c and 3.4d indicating that K can be fairly well constrained by resistivity data - a consequence of the fact that the porosity is fixed to produce these images, thereby avoiding the tradeoffs seen in Figures 3.4a-b. In contrast, the voltage RMSD increases much more slowly as dispersivity is varied from its reference value, suggesting that uniquely constraining α_x with resistivity data would be more difficult. The same type of behavior is seen in Figure 3.4e and 3.4f when porosity is varied with dispersivity. In both cases, the voltage RMSD increases to approach the value calculated for background aquifer conditions, i.e. no plume present, as the dispersivity is increased and the fixed mass of the plume is spread over an increasingly larger region, leading to lower concentrations at any particular location. We choose to focus, however, on the small range of dispersivity shown in Figure 3.4 (α_x = 0.05-0.5m) to highlight an important issue that could affect optimization of the transport parameters. Specifically, in both Figures 3.4c-d and 3.4e-f, the RMSD minima appear to branch to form a V-shape as the

dispersivity is increased from the reference value, though the effect is stronger for the case where the current electrodes are perpendicular to the flow direction due to the smaller electrode separation. The similarity of the RMSD response observed in Figures 3.4c-f suggests that there is a fundamental tradeoff between dispersivity and flow velocity, which control the size and position of the plume, respectively. As a result, varying dispersivity and velocity along a path with fixed RMSD considerably changes the subsurface concentration distribution. The RMSD tradeoffs in Figures 3.4c-f are therefore caused by the electrical equivalence of different plumes in the subsurface. This is in contrast to the case in Figure 3.4a-b where the fixed values of K/n produce an equivalent concentration plume.

3.5 Discussion

Evaluating the transport conditions under which different plumes produce an electrically equivalent resistivity response is a fundamentally important issue for calibrating flow models with resistivity data. While multi-electrode surveys are commonly used for imaging purposes, it is difficult to separate the information content contributed by each measurement for constraining the transport parameters in the context of coupled inversion. We therefore investigate the electrical equivalence problem by calculating the apparent resistivity for a single set of current and potential electrodes, in this case using a Wenner array [Wenner 1912a, 1912b] perpendicular to the flow direction with a 10m electrode separation. Apparent resistivity is a good measure of equivalence between individual resistivity measurements since it captures the average

resistivity of the subsurface as sensed by the electrodes. In all calculations the simulation time is fixed at 83.3hrs, such that the plume is centered between the electrodes for the reference set of transport parameters (Table 3.1).

Table 3.1: Parameter values used in analyses.

Parameter	**Symbol**	**Value**	**Units**
Reference hydraulic conductivity	K^{ref}	1×10^{-4}	meters/second
Reference porosity	n^{ref}	0.3	volume/volume
Reference longitudinal dispersivity	α_x^{ref}	0.1	meter
Hydraulic head gradient	dh/dx	1	length/length
Background concentration	c_{bg}	0.1461	grams/Liter
Applied voltage (for objective function analyses)	V_{app}	20	Volts
Injected current (for apparent resistvity calculations)	I_{inj}	0.01	Amperes/meter
Mass input (for objective function analyses)	M	65	kilograms
Sample Rate	S	2×10^{-3}	Hertz
Best times (current pair in-line with flow)	bt_1	74.31 to 75.56	hours
Best times (current pair perpendicular to flow)	bt_2	74.72 to 75.97	hours

Figure 3.5 shows the results of the additional examinations run to take a closer look at the trade-off between longitudinal plume location which is controlled by K and n, and the spatial extents of the plume which is controlled by α. Figure 3.5a is a plot of K versus ρ_{app} where the level curves are values of α_x, the purple dashed line is the value of K^{ref}, and the blue dashed line indicates the static ρ_{app} prior to injection where the c_{bg} = 0.1461 g/L (i.e. ambient background concentration and no plume present). The solid and dashed ax level curves are differentiated to be indicative of the α_x value where the ρ_{app} response magnitude begins to reduce due to dispersion that causes c to approach c_{bg}. Figure 3.5b is a plot of maximum plume concentration versus ρ_{app} where the solid and dashed level curves are measures of α_x and M respectively. The red, black, and blue dashed lines are bounding lines that refer to the c_{bg}, true resistivity calculated using

Archie's Law ($\rho_{Archie's}$), and the static background resistivity with $c = c_{bg}$ respectively. The points are locations in parameter space that results are extracted from a single model run.

The change in apparent resistivity as a function of plume position and size, controlled via hydraulic conductivity and dispersivity, respectively, is shown in Figure 3.5a. The maximum changes in apparent resistivity occur when the center of the plume is centered between the electrodes. As the hydraulic conductivity is either increased or decreased the plume is moved off-center of the electrodes and the apparent resistivity increases until the plume is no longer within the zone of sensitivity of the electrodes and the apparent resistivity equals the background value. The effect of dispersivity, i.e., plume size, on apparent resistivity is also dramatic as apparent resistivity decreases as the plume grows. A very compact plume resulting from an aquifer with a low dispersivity takes up a small fraction of the measurement volume between the electrodes. The apparent resistivity is therefore low because it reflects an average of the background and plume resistivities. In contrast, current flow can be channeled through a conductive plume when the size of the plume becomes comparable to the electrode spacing, leading to lower apparent resistivities. Note, however, that as the plume is dispersed the solute concentrations also decrease, so there is a limit to this behavior. Figure 3.5b shows that large, but dilute plumes, i.e., high dispersivity, can produce apparent resistivity responses similar to compact, concentrated plumes, i.e., low dispersivity. An important inference from Figure 3.5a is that there is range of hydraulic conductivity and dispersivity values that produce exactly the same apparent resistivity response. The reason is because a shift

in the position of the plume can be offset by increasing the size of the plume. This is the fundamental reason for the tradeoff between dispersivity and hydraulic conductivity shown in Figure 3.4c-d.

Because dispersion affects solute concentrations, which directly influence subsurface resistivity, it was further explored whether non-unique apparent resistivity responses can be obtained by varying dispersivity and the mass of solute injected into the subsurface. Figure 3.5b shows that there is a relatively complex relationship between the size of the plume and the solute concentrations. Note that for all calculations in Figure 3.5b the plume was centered on the electrodes. For low dispersivity values, the plume is small relative to the electrode spacing and a minimal change in apparent resistivity from the background is observed, even for extremely high solute concentrations. As the plume increases in size, the apparent resistivity becomes much more sensitive to solute concentration and less dependent on dispersivity values. At high dispersivity values, the plume is much larger than the electrode spacing and the solute concentration is effectively homogeneous in the zone of measurement sensitivity. The apparent resistivity therefore decreases with increasing concentration following Archie's law and there is no information about dispersivity contained in the data.

a)

b)

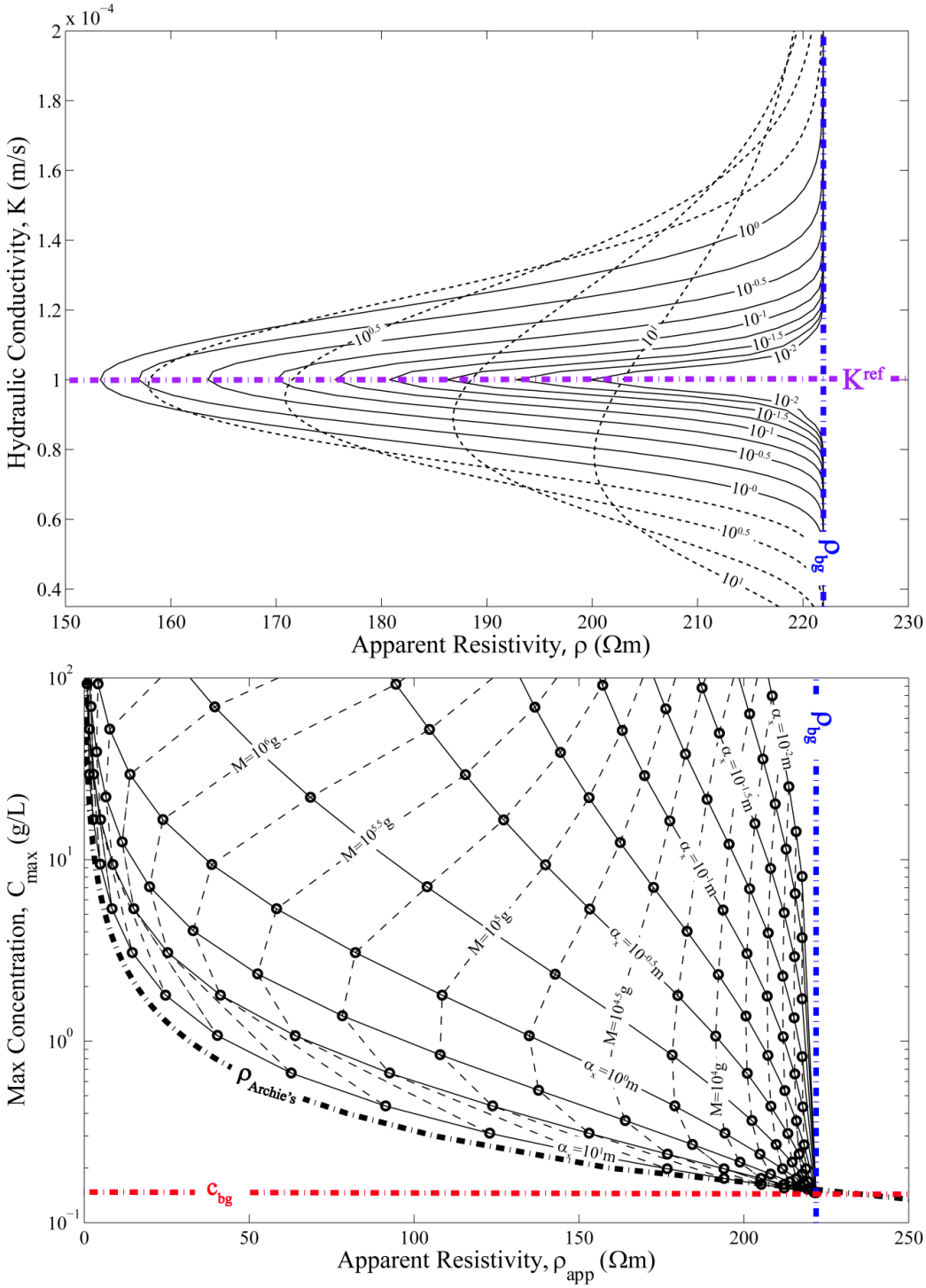

Figure 3.5: Hydraulic conductivity (a) and max concentration (b) vs. apparent resistivity with variations in longitudinal dispersivity. The level lines in (a) represent different values of α_x. Background resistivity, ρ_{bg}, is a reference to the apparent resistivity with only background concentrations in the study area (i.e. no tracer in the area of influence). True resistivity, $\rho_{Archie's}$, is the resistivity calculated using Archie's Law for varied values of concentration. Background concentration, c_{bg}, remains at 0.1461 g/L.

3.6 Conclusions

The goal of this study was to evaluate whether surface-based electrical resistivity data could provide a constraint on aquifer flow and transport parameters. To evaluate this issue, synthetic electrical resistivity surveys were conducted to monitor a tracer test. The study shows that surface-based electrical resistivity surveys could provide a powerful means for estimating aquifer flow and transport properties if these data are sensitive to the survey. The voltage responses calculated at each location in the subsurface as a function of the transport parameters (K, n, and α_x) were compared to a synthetic reference case and used to evaluate how the transport parameters influence IDF estimations. Though the results may not be universally applicable, some trends arose that could likely be applied to similar hydrogeophysical problems:

1. K and n define the flow velocity. Through knowledge of this relationship and its implications to timing, a good estimate of K/n is possible using only surface voltage and hydraulic head measurements.
2. A trade-off occurs between K and n, but can be overcome due to dependence of n in Archie's law.
3. α may remain difficult to constrain because of the resistivity data are not unique to any single α. There are tradeoffs between tracer mass, dispersion, and spatial location that may be possible to further constrain with the addition of more observational data that corresponds to the insertion of additional current electrode pairs.

3.7 References

Archie, G. E. (1942), The electrical resistivity log as an aid in determining some reservoir characteristics, *Trans. Am. Inst. Min. Metall. Pet. Eng.*, 146, 54– 62.

Binley, A., S. Henry-Poulter, B. Shaw (1996), Estimation of solute transport in an undisturbed soil column using electrical resistance tomography, *Water Resources Research*, vol. 32, no. 4, pp. 763-769.

Binley, A., G. Cassiani, R. Middleton, P. Winship (2002), Vadoze zone flow model parameterisation using cross-borehole radar and resistivity imaging, *Journal of Hydrology*, vol. 267, no. 3-4, pp. 147-159.

Comsol Multiphysics 3.5a: User's Guide (2008), www.comsol.com.

Daily, W., A. Ramirez, D. LaBrecque, J. Nitao (1992), Electrical resistivity tomography of vadoze water movement, *Water Resources Research*, vol. 28, no. 5, pp. 1429-1442.

Darcy, H. (1856), *Les fontaines publiques de la ville de Dijon*. Paris: Victor Dalmont.

Day-Lewis, F. D., K. Singha, A. M. Binley (2005), Applying petrophysical models to radar travel time and electrical resistivity tomograms: Resolution-dependent limitations, *Journal of Geophysical Research*, vol. 110, B08206.

Freeze, R. A., J. A. Cherry (1979), *Groundwater*. Prentice Hall, Englewood Cliffs, N.J., 604p.

Gelhar, L. W. , C. Welty, K. R. Rehfeldt (1992), A critical review of data on field-scale dispersion in aquifers, *Water Resources Research*, vol. 28, no. 7, pp. 1955-1974.

Hinnell, A. C. , T. P. A. Ferre, J. A. Vrugt, J. A. Huisman, S. Moysey, J. Rings, M. B. Kowalsky (2010), Improved extraction of hydrologic information from geophysical data through coupled hydrogeophysical inversion, *Water Resources Research*, vol. 46, W00D40.

Huisman, J. A, J. Rings, J.A. Vrugt, J. Sorg, H. Vereecken (2010), Hydraulic properties of a model dike from coupled Bayesian and multi-criteria hydrogeophysical inversion, *Journal of Hydrology*, vol. 380, pp. 62–73.

Kemna, A., J. Vanderborght, B. Kulessa, and H. Vereeken (2002), Imaging and characterisation of subsurface solute transport using electrical resistivity tomography (ERT) and equivalent transport models, *Journal of Hydrology*, vol. 267, no. 3-4, pp. 125-146.

Koestel J., J. Vanderborght, M. Javaux, A. Kemna, A. Binley, and H. Vereecken (2009), Noninvasive 3-D transport characterization in a sandy soil using ERT: 1. Investigating the validity of ERT-derived transport parameters, *Vadoze Zone Journal*, vol. 8, no. 3, pp. 711-722.

Koestel, J., A. Kemna, M. Javaux, A. Binley, H. Vereecken (2008), Accounting for spatially variable resolution in electrical resistivity tomography through field-scale rock-physics relations, *Geophysics*, vol. 71, no. 4, pp. A25–A28.

Kowalsky, M. B., S. Finsterle, J. Peterson, S. Hubbard, Y. Rubin, E. Majer, A. Ward, G. Gee (2004), Estimation of field-scale soil hydraulic and dielectric parameters through joint inversion of GPR and hydrological data, *Water Resources Research*, vol. 41, W11425.

Kowalsky, M. B., S. Finsterle, Y. Rubin (2005), Estimating flow parameter distributions using ground-penetrating radar and hydrological measurements during transient flow in the vadose zone, *Advances in Water Resources*, vol. 27, pp. 583–599.

Lambot, S., E. C. Slob, M. Vanclooster, H. Vereecken (2006), Closed loop GPR data inversion for soil hydraulic and electric property determination, *Geophysical Research Letters*, vol. 33, no. 21, L21405.

Lenda, A., A. Zuber (1970), Tracer dispersion in groundwater experiments, *Proceedings of a Symposium on the Use of Isotopes in Hydrology*, I.A.F.A., Vienna, pp. 619-641, Mar. 9-13.

Lesmes, D. P., S. P. Friedman (2005), Relationships between the electrical and hydrogeological properties of rocks and soils, In: Rubin, Y, S. S. Hubbard (eds) *Hydrogeophysics*, *Chapter 4*, Springer, Dordrecht, The Netherlands, pp 87–128.

Linde, N., A. Binley, A. Tryggvason, L. B. Pedersen, A. Revil (2006), Improved hydrogeophysical characterization using joint inversion of cross-hole electrical resistance and ground-penetrating radar traveltime data, *Water Resources Research*, vol. 42, W12404.

Looms, M. C., A. Binley, K. H. Jensen, L. Nielsen, T. M. Hansen (2008), Identifying unsaturated hydraulic parameters using an integrated data fusion approach on cross-borehole geophysical data, *Vadoze Zone Journal*, 7(1), 238-248.

Moysey S., R. J. Knight, K. Singha (2006), Relating geophysical and hydrologic properties using field-scale rock physics, *CMWR XVI -- Computational Methods in Water Resources*, Copenhagen, Denmark, 8p.

Moysey, S., D.E. Fowler, T. Sicilia (2007), Impact of Integrated Versus Sequential Data Fusion on Hydrologic Predictions, *Eos Trans. AGU*, 88(52), Fall Meet. Suppl., Abstract H41H-03.

Moysey, S., K. Singha, R. Knight (2005), A framework for inferring field-scale rock physics relationships through numerical simulation, *Geophysical Research Letters*, 32, L08304.

Olsen, P. A., A. Binley, S. Henry-Poulter, W. Tych (1999), Characterizing solute transport in undisturbed soil cores using electrical and X-ray tomographic methods, *Hydrological Processes*, vol. 13, no. 2, pp. 211-221.

Rucker, D. F., T. P. A. Ferre (2004), Parameter estimation for soil hydraulic properties using zero-offset borehole radar: Analytical method, *Soil Science Society of America Journal*, vol. 68, pp. 1560-1567.

Singha, K., S. M. Gorelick (2006), Effects of spatially variable resolution on field-scale estimates of tracer concentration from electrical inversions using Archie's law, *Geophysics*, vol. 71, no. 3, pp. G83-G91.

Singha, K., S. M. Gorelick (2005), Saline tracer visualized with three-dimensional electrical resistivity tomography: Field-scale spatial moment analysis, *Water Resources Research*, vol. 41, W05023.

Singha, K., S. Moysey (2005), Accounting for spatially variable resolution in electrical resistivity tomography through field-scale rock-physics relations, *Geophysics*, vol. 71, no. 4, pp. A25-A28.

Slater L., A. M. Binley, W. Daily, R. Johnson (2000), Cross-hole electrical imaging of a controlled saline tracer injection, *Journal of Applied Geophysics*, vol. 44, pp. 85-102.

Slater, L. D., S. K. Sandberg (2000), Resistivity and induced polarization monitoring of salt transport under natural hydraulic gradients, *Geophysics*, vol. 65, no. 2, pp. 408–420.

Uhlenbrook, S., J. Didszun, J. Wenninger (2008), Source areas and mixing of runoff components at the hillslope scale - a multi-technical approach, *Hydrological Sciences Journal*, vol. 53, no. 4, pp. 741-753.

Wenner, F. (1912a), The four-terminal conductor and the Thompson Bridge, *U. S. Bureau of Standards Bulletin*, vol. 8, pp. 559-610.

Wenner, F. (1912b), A method of measuring earth resistivity, *U. S. Bureau of Standards Bulletin*, vol. 12, pp. 469-478.

CHAPTER 4

ASSESSMENT OF THE ROLE OF CONCEPTUAL MODEL ERROR IN INTEGRATED DATA FUSION

4.1 Abstract

It has been shown previously that transient resistivity data collected during a tracer test can be used within the integrated data fusion (IDF) framework to constrain hydrologic parameters for a coupled hydrologic and geophysical model. An underlying assumption of that work, however, is that the structure of the hydrologic model is known and correctly represents true transport processes. I now evaluate whether geophysical data are sensitive to the choice of an incorrect model structure, i.e., hydrologic conceptual errors. A numerical study is performed to evaluate whether synthetic resistivity data generated for flow through heterogeneous materials can be reproduced when it is incorrectly assumed that the subsurface is homogeneous. In this study two different heterogeneous scenarios are investigated. In both cases a low permeability zone is embedded within a homogeneous background material. In the first scenario the low permeability zone is located at the ground surface, forcing the tracer to follow a deep flow path far from the electrodes of the resistivity survey. In the second scenario the low permeability zone is shifted downward, having the effect of forcing the tracer above it toward the electrodes at the ground surface. A series of tests are conducted to determine how well, if at all, a homogeneous model can fit the electrical resistivity data generated by each heterogeneous scenario utilizing only a sparse quantity of electrodes (i.e. one

current-potential pair, and three current-potential pairs). The results of this study indicate that there may not be enough information contained with the one current-potential pair simulation to definitively rule out the possibility that the system is homogeneous.

4.2 Introduction

The interpretation strategy utilized in this research, known as Integrated Data Fusion (IDF) [Moysey et al., 2006], coupled inversion [Ferre et al., 2009] or closed-loop inversion [Lambot, et al., 2006], links hydrological and geophysical models to directly estimate hydraulic parameters of the subsurface using transient geophysical data. IDF can be utilized with resistivity data for improved estimation of flow and transport parameters of the aquifer.

The IDF method (Figure 4.1) consists of multiphysics simulation that couples hydrologic and geophysical models to link hydrologic parameters to geophysical observations. Hydrologic parameters to be estimated (i.e. hydraulic conductivity, K; porosity, n; dispersivity, α) are input into the hydrologic simulation module of which hydrologic properties such as hydraulic gradient and concentration are output. Using rock physics relationships the hydrologic properties are converted to geophysical properties. The geophysical properties are then input into the geophysical simulation module and the final output are the simulated geophysical data. The outputs (e.g. V, ρ_{app}) of the multiphysics model are then input into a parameter estimation algorithm where the data misfit is reduced to some predetermined threshold. The outputs of the IDF workflow are hydrologic parameter estimates.

Creating a hydrologic conceptual model (HCM) is accomplished by determining the significant subsurface attributes (e.g. facies distributions) and physical processes (e.g. flow, transport, and resistivity), and then integrate them into a simplified representation of the hydrogeologic system. This simplistic theoretical description, or HCM, can include site specific field observations and generalizations about the formation, among other things. The HCM can then be used to develop a simulation model, whether it is analytical or numerical, that will be the focus of a series of tests to determine model suitability for the system under investigation using tools like parameter estimation.

Previous work has focused on parameter sensitivity for a homogeneous system (i.e. a system in which there is no spatial variability in properties) and where the spatial distribution of hydrologic properties, is assumed to be known. The question raised in this chapter is: **What are some consequences of incorrectly conceptualizing the hydrologic model?**

Though there is a rather limited account in scientific literature of what happens when the HCM is inaccurate, we have assumed that it often occurs in instances where hydrologic parameters are inferred from geophysical data. Corollary to this, in a series of examples using hydrologic data to constrain the HCM, Gaganis and Smith [2001 and 2006] quantify error associated with the HCM, or conceptual error, by evaluating the spatial and temporal variations in model error. Gaganis and Smith state that the cause of the hydrologic model error is that a mathematical representation of a physical system is flawed, but in a systematic manner. Hinnell et al. [2010] gives an examination of coupled hydrogeophysical inversion (same as IDF) which shows that when the model is

an accurate representation of the true system, the coupled approach can reduce uncertainty. Likewise, it is shown that when the physical system is incorrectly conceptualized, there can be fundamental defects in the analysis.

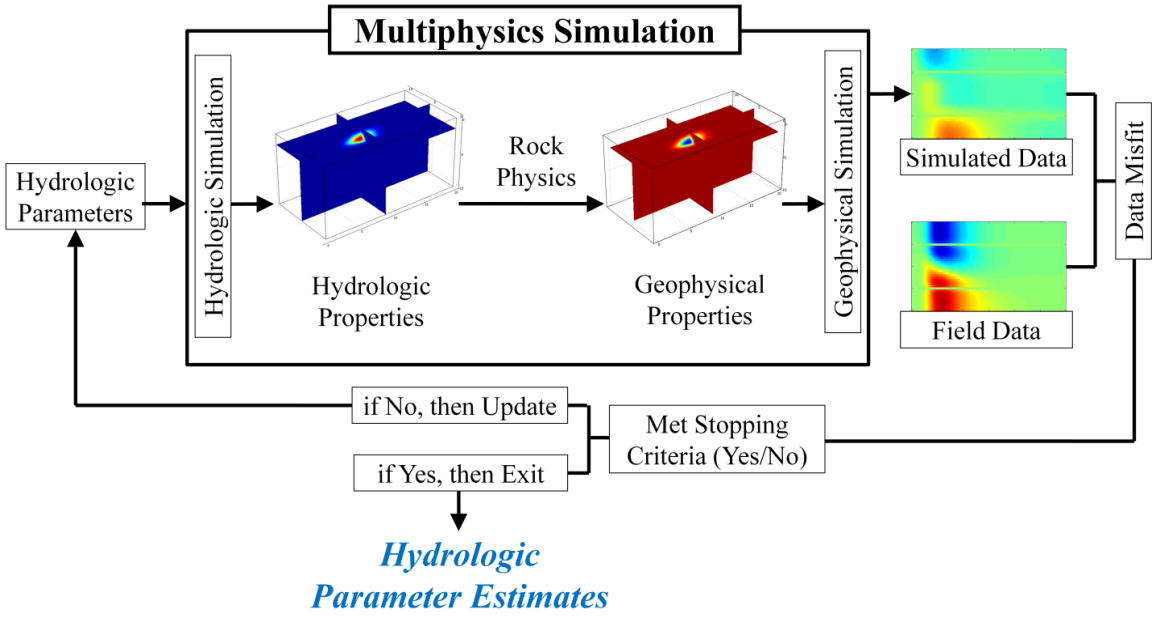

Figure 4.1: Flow schematic describing the integrated data fusion (IDF) workflow. The hydrologic and geophysical simulations, coupled by rock physics relationships, comprise the multiphysics simulation. Hydrologic parameters are the input and simulated geophysical data are output of the multiphysics simulation. The simulated geophysical data and field data are then used to compute the model data misfit. If a maximum misfit threshold condition is met, the hydrologic parameter estimates are output.

The objective of this research is to evaluate whether the use of an incorrect HCM in the IDF framework can lead to misinterpretation of the aquifer parameters estimated from resistivity monitoring data collected during a tracer test. To this end, two simple heterogeneous scenarios are investigated where the tracer is either forced away from or towards the surface where the electrodes are located. The transient resistivity data obtained for each of these scenarios are then used in the IDF framework to estimate the transport parameters for an equivalent homogeneous model to determine the impact of

conceptual error (i.e. to see how closely the homogeneous-*K* model can match resistivity data from the heterogeneous-*K* models).

4.3 Methods

4.3.1 Model Overview

The purpose of this study, to investigate the sensitivity of resistivity data collected during a tracer test to changes in a HCM, will be explored using data generated from numerical models in the finite element software COMSOL Multiphysics [COMSOL, 2008]. For this purpose, three different conceptual models will be considered (Figure 4.2). One system is homogeneous and the other two are simplistic heterogeneous models with a low-*K* block either forcing the tracer towards or away from the electrode array or the near-surface. An analysis was conducted to determine if a set of model parameters can be found for the homogeneous conceptual model that yield similar resistivity data as one or both of the heterogeneous models.

The two-dimensional geometry (Figures 4.2a, 4.2b, and 4.2c) is rectangular with L_x = 20m and L_z = 10m. For simplicity, there is no vadoze zone which best represents the case where there is a shallow water table and the electrodes protrude into the saturated zone. The Darcy's Law and transient Solute Transport modules from the Earth Science module are used to simulate groundwater flow and transport, respectively. The DC Electrical Conductivity module is used to simulate current injection and the resultant voltage distributions for the electrical resistivity survey.

4.3.2 Flow and Transport Models

The flow and transport for this two-dimensional analysis assumes steady-state flow under uniform mean hydraulic (Figure 4.2). Groundwater flow is governed by the groundwater flow equation

$$\nabla \cdot (\mathbf{K} \nabla h) = 0 , \tag{4.1}$$

where **K** is the hydraulic conductivity tensor and *h* is the hydraulic head. Given the hydraulic gradient, ∇h, the velocity, **v**, can be determined using a modified form of Darcy's Law [Darcy, 1856] that accounts for effective porosity n_e [Fetter, 2001]

$$\mathbf{v} = \frac{-\mathbf{K} \nabla h}{n_e} . \tag{4.2}$$

The solution to Equation 4.2 can then be used to calculate the concentrations at any location in 2D Cartesian space [Bear, 1979] by

$$\frac{\partial C}{\partial t} = -\nabla \cdot (\mathbf{v} C - \mathbf{D} \cdot \nabla C) , \tag{4.3}$$

where *C* is solute concentration, **D** is the dispersion coefficient tensor, and **v** is the variable flow velocity. The hydrodynamic dispersion term (x-direction for Equation 4) can then be expressed as

$$D_x = \alpha_x v_x + D_d , \tag{4.4}$$

where α_x is the longitudinal dispersivity (α_z corresponds to vertical dispersivity) and D_d is the molecular diffusion coefficient, which is generally negligible.

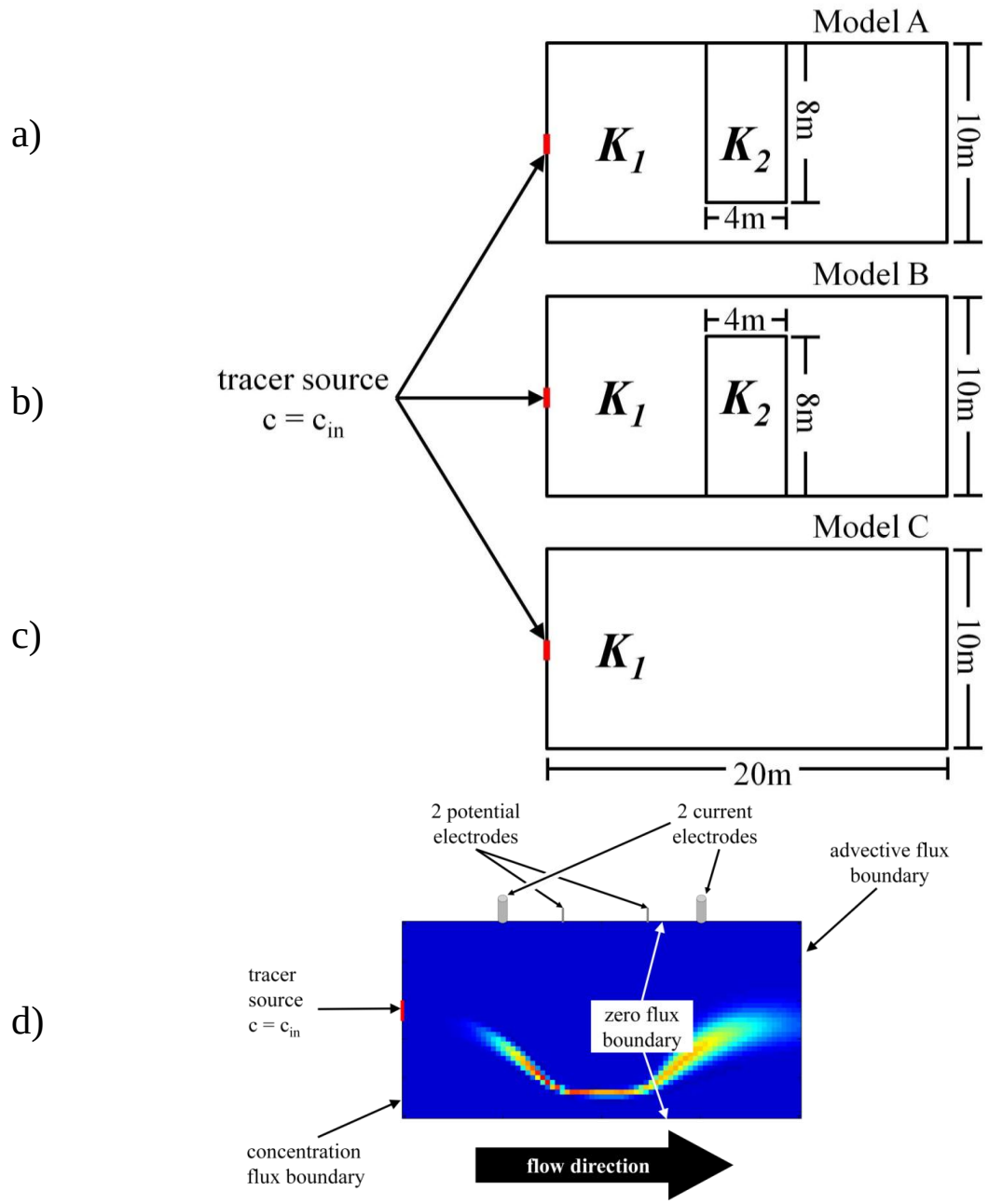

Figure 4.2: Geometry for heterogeneous model that forces (a) away from the surface and (b) towards the surface, (c) the homogeneous model, and (d) transport boundary conditions, electrode configuration, and flow direction showing tracer flow path for Model A.

The tracer injection location is a 1m boundary patch on the upstream face ($x = 0$) with a center point located halfway down the z-axis. The tracer patch is set to have a

fixed concentration of 29.22 g/L for the initial hour of the experiment. Subsequent to the injection, the tracer patch reverts to the background concentration, c_{bg}, which is 146.1 mg/L and remains at the background value for the entire duration of the experiment. The right face is an advective flux boundary and the upper and lower faces are zero flux.

4.3.3 Rock Physics and Archie's Law

The transport module's output is concentration, which must first be converted to bulk electrical resistivity before being input into the resistivity module. This is done by using Archie's Law [Archie, 1942], which is an empirical formula that relates resistivity of pore fluids, ρ_w to the bulk resistivity of the formation, ρ_b. For the case where the porous media is fully saturated Archie's Law is

$$\rho_{eff} = aF\rho_w , \tag{4.5}$$

where the formation factor, $F = n^{-m}$, is a constant that relates the resistivity of the rock to the resistivity of the pore water and a is an empirical scaling factor. The formation factor consists of the porosity, n, and the cementation factor, m, which is related to the tortuosity of the rock. To obtain ρ_w from the solute concentration, c (mg/L), in these numerical experiments, the relationship between total dissolved solids and fluid electrical resistivity from Lesmes and Freidman [2005] is used:

$$\rho(x,y,z,t) = 6.7 \text{ x } 10^{3} n^{1.3} c(x,y,z,t) . \tag{4.6}$$

Here, the cementation factor is 1.3.

4.3.4 Resistivity Model

The voltage (V) distribution in the subsurface is governed by

$$\nabla \cdot \left(\frac{1}{\rho} \nabla V \right) = 0 \tag{4.7}$$

The model design utilizes a Wenner [Wenner, 1912a, 1912b] dipole-dipole survey geometry, with a single pair of current and potential electrodes. The current electrodes are located on the ground surface (y = 0) at locations of x = 5m and 15m for the positive and negative electrodes respectively. The magnitude of current injection, I_{inj}, is 10^{-5} A/m. The potential electrodes are used to sample the temporal variations of the electric field caused by the movement of the saline tracer. The two potential electrodes are equally spaced between the current electrodes at 8.3m and 1.7m. Using this spacing the apparent resistivity can be calculated using

$$\rho_{app} = \kappa \frac{\delta V_{MN}}{I_{inj}} = \kappa R, \tag{4.8}$$

where κ is the electrode array geometric factor and R is the resistance, where δV_{MN} is the voltage difference between the two potential electrodes and I_{inj} is the current injected at the current electrodes. In general, the Wenner array $\kappa = 2\pi L_a$ = 20.9m, where L_a, the electrode spacing, is 3.33m. However, this geometric factor is for a three-dimensional system. For the two-dimensional system considered here, the κ is determined empirically. The κ for this specific case, 1.88m, is given by Equation 4.9 and is determined using simulations in a homogeneous background where $\rho_{Archie's}$ is the true

resistivity and δV_{MN} is the voltage difference calculated between the two potential electrodes.

$$\kappa = \frac{\rho_{Archie's} I_{inj}}{\delta V_{MN}}, \tag{4.9}$$

4.3.5 Evaluation of data sensitivity

The heterogeneous models (Figure 4.2a and 4.2b) are run for the reference case where the input parameters (Table 4.1) do not vary spatially with the exception of the reference *K*, where $K_1^{ref} = 10^{-4}$ m/s and $K_2^{ref} = 10^{-8}$ m/s for the high and low-*K* zones respectively. The reference models were run for 50 hours with time steps set to 8.3 minutes for fixed output times. The outputs are concentrations and voltages at each time step. Then the ρ_{app} versus time was determined using Equations 4.10.

Table 4.1: Parameter values used in analyses.

Parameter	**Symbol**	**Value**	**Units**
Reference hydraulic conductivity #1	K_1^{ref}	1 x 10^{-4}	m/s
Reference hydraulic conductivity #2	K_2^{ref}	1 x 10^{-8}	m/s
Reference porosity	n^{ref}	0.3	m3/m3
Reference longitudinal dispersivity	α_x^{ref}	0.1	m
Reference vertical dispersivity	α_z^{ref}	0.001	m
Hydraulic head gradient	∇h	1	m/m
Background concentration	c_{bg}	0.1461	g/L
Injected current (for apparent resistvity calculations)	I_{inj}	1 x 10^{-5}	A/m
Tracer concentration	C_{in}	29.22	g/L
Geometric Factor	κ	1.88	m

The examination of these cases is in three parts:

1. *Test the correct conceptual models to determine how sensitive the resistivity data are to the two model sub-domains*. An objective function analysis is conducted for this purpose where Model A and B (Figures 4.2a/b) are run for variations in only K_1^{ref} and K_2^{ref} to determine whether the resistivity data coupled with the correct conceptual model can constrain the two *K*-values. The objective function is defined by root mean squared error (RMSE) between the simulated apparent resistivity response for trial values of the parameters, i.e., $\rho_{app(i)}(K_1, K_2)$, and the apparent resistivity calculated in the reference data set, i.e., $\rho_{app(i)}^{ref} = \rho_{app(i)}(K_1^{ref}, K_2^{ref}, n^{ref}, \alpha_x^{ref}, \alpha_z^{ref})$:

$$E(\rho_{app}) = \left[\frac{1}{N_t} \sum_{i=1}^{N_t} (\rho_{app(i)}(K_1, K_2) - \rho_{app(i)}^{ref})^2 \right]^{0.5}, \qquad (4.10)$$

Here the total number of observation times is $N_t = 10$. The observation times are chosen from the reference data by picking the maximum ten values of $\Delta\rho_{app}^{ref}$ using $\Delta\rho_{app(i)}^{ref} = \rho_{app(i)}^{ref} - \rho_{app(t=0)}^{ref}$. All parameters other than K_1 and K_2 are assumed to be known.

2. *Test the homogeneous model (Model C) to determine how changes in each principal parameter affect the ρ_{app} signal, thus exploring the potential of these variations to affect an optimization using an incorrect conceptual model*. To this end, Model C (Figure 4.2c) is run for the reference values of K_1, n, α_x, and α_z, where the reference values used are the same as in the Model A and B reference cases (Table 4.1). Model C is then run again for factor of two variations in *K* and

n and factor of ten variations of α_x and α_z ranging from 10^{-4} to 10^0 m, while keeping the unvaried parameters at the reference value. This is done to determine how the timing, magnitude, and shape of the heterogeneous models' ρ_{app} signal could be mirrored without the presence of the low-K zone.

3. *A Parameter ESTimation (PEST) [Doherty, 2004] optimization for K, n, and α_x is conducted for Model A and B, using the homogeneous model (Model C).* In the optimization for Model A and Model B - test 1 α_z is tied to α_x by $\alpha_z = 0.01\alpha_x$. In the optimization for Model B - test 2 the two dispersivity values are untied to better match the large magnitude change in the ρ_{app} signal. The simulation times (37 in total) for the optimization are chosen by running the model from the start time, t_0, to $t = t(\Delta\rho_{max})$, which is the time where the maximum change in ρ_{app} occurs using time steps of t_{step} = 83.3 minutes. Then the simulation times go from $t(\Delta\rho_{max})$ by t_{step} to the point where ρ_{app} approaches, or is approximately equal to ρ_{bg}. The objective function utilized in these PEST runs is the sum of squared difference in apparent resistivities (SSρD) given the reference ρ_{app}, i.e., $\rho_{app(i)}^{\text{ref}} = \rho_{app(i)}(K^{ref}, n^{ref}, \alpha_x^{ref}, \alpha_z^{ref})$, and the ρ_{app} response calculated for a set of test hydrologic parameters, $\rho_{app(i)} = \rho_{app(i)}(K, n, \alpha_x, \alpha_z)$:

$$E(\rho_{app}) = \sum_{i=1}^{N_t} (\rho_{app(i)}(K, n, \alpha_x, \alpha_z) - \rho_{app(i)}^{ref})^2 , \qquad (4.11)$$

Here N_t is the total number of observation times. There was not data weighting included, therefore all the data misfits have the potential to affect the objective function equally.

4.4 Results

Figure 4.3 displays the objective function surface, K_2 versus K_1 for Model A (a) and B (b) using the correct HCM for each. The color scale is the RMSE in ρ_{app} where the white, or RMSE = 0, corresponds to a data misfit of zero in comparison to the reference case and black corresponds to the maximum RMSE in the data. The results of the objective function analysis using the correct HCM indicate that for each case there is parameter insensitivity to the low-*K* zone, seen by the low RMSE value that transects K_2 from 10^{-10} to 10^{-5} m/s. This is significant due to the data insensitivity evident even when there is knowledge of the subsurface facies distributions. In this case, the data insensitivity is caused by the large difference between the *K*-values effectively producing a no-flow zone from the low-*K* zone; at a K_2 value less than 10^{-5}, the flow paths for the plume are routed around the low-*K* inclusion regardless of how impermeable it is.

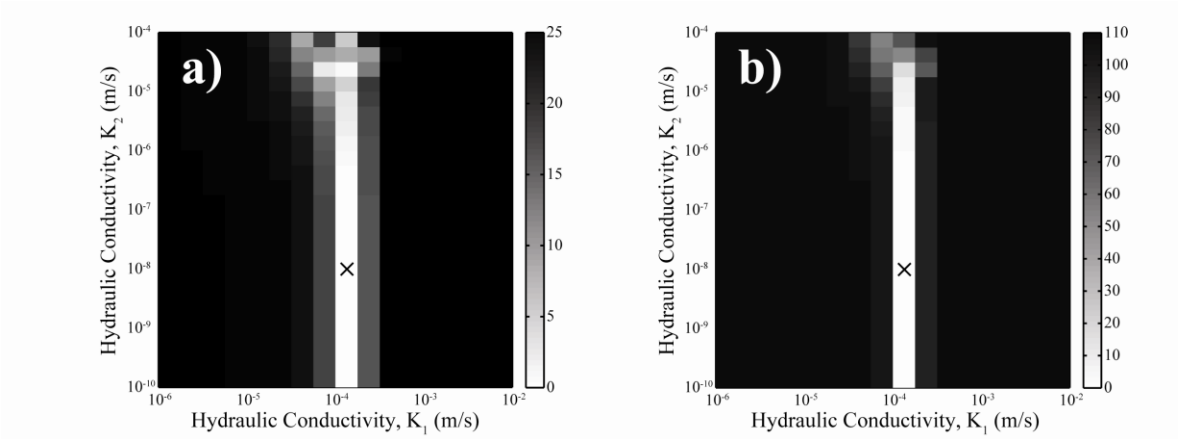

Figure 4.3: RMSE objective function surface with variations in K_1 and K_2 using the correct conceptual models where a) Model A forces the tracer towards the surface and b) Model B forces the tracer away from the surface. The black 'X' in each figure represents the location of the reference parameter pair.

Figure 4.4 shows the curves for the sensitivity analysis using homogeneous Model C in ρ_{app} versus time for variations in: a) *K*, b) *n*, c) α_x, and d) α_z. In 4.4a/b the solid

black, dashed blue, and dashed pink lines represent the reference value case, the reference parameter decreased by a factor of two, and the reference value increased by a factor of two respectively. In 4.4c/d, the solid black lines represent the reference value case, where the variations, shown in the dashed lines, are in factors of ten ranging from 10^{-4} to 10^{0} m for both α_x and α_z. The results of the homogeneous parameter sensitivity analysis which was conducted to determine how the ρ_{app} signal can vary even without the addition of the low-K inclusion, indicate that as *K* increases and *n* decreases, there is a shift of the apparent resistivity signal forward in time. Also of note regarding the *K* and *n* variations in Figure 4.4a/b, are the magnitude and width of the ρ_{app} signal differences. These changes are artifacts of how the tracer is included in the model at a concentration boundary, and are therefore directly tied to groundwater velocity and affects the size and total mass of the plume that enters the system.

As α_x increases (Figure 4.4c), there is a lengthening of the response time and increase in magnitude of the tracer's response in the resistivity signal. The lengthening of the response time corresponds directly to the size increase of the plume in the longitudinal direction, while the increase in ρ_{app} magnitude is related to the overall change in the size of the plume caused by an increased dispersion, thus causing an increase in its geo-electrical "footprint."

As α_z increases (Figure 4.4d), the magnitude of the ρ_{app} magnitude increases greatly due to the vertical stretching of the plume, which causes it to get closer to the surface electrodes, thus having a greater influence on the "apparent" resistivity of the system. Of particular note in this case, when $\alpha_z = 10^{0}$ m, the plume is dispersed so much

in the vertical direction that it begins to influence the electrode directly. This direct influence causes the deviation from the smooth, continuous bell-shaped ρ_{app} signal to a signal that appears to contain three signals superimposed upon one another, though the maximum ρ_{app} response remains at the time when the plume is centered between the current electrode pair.

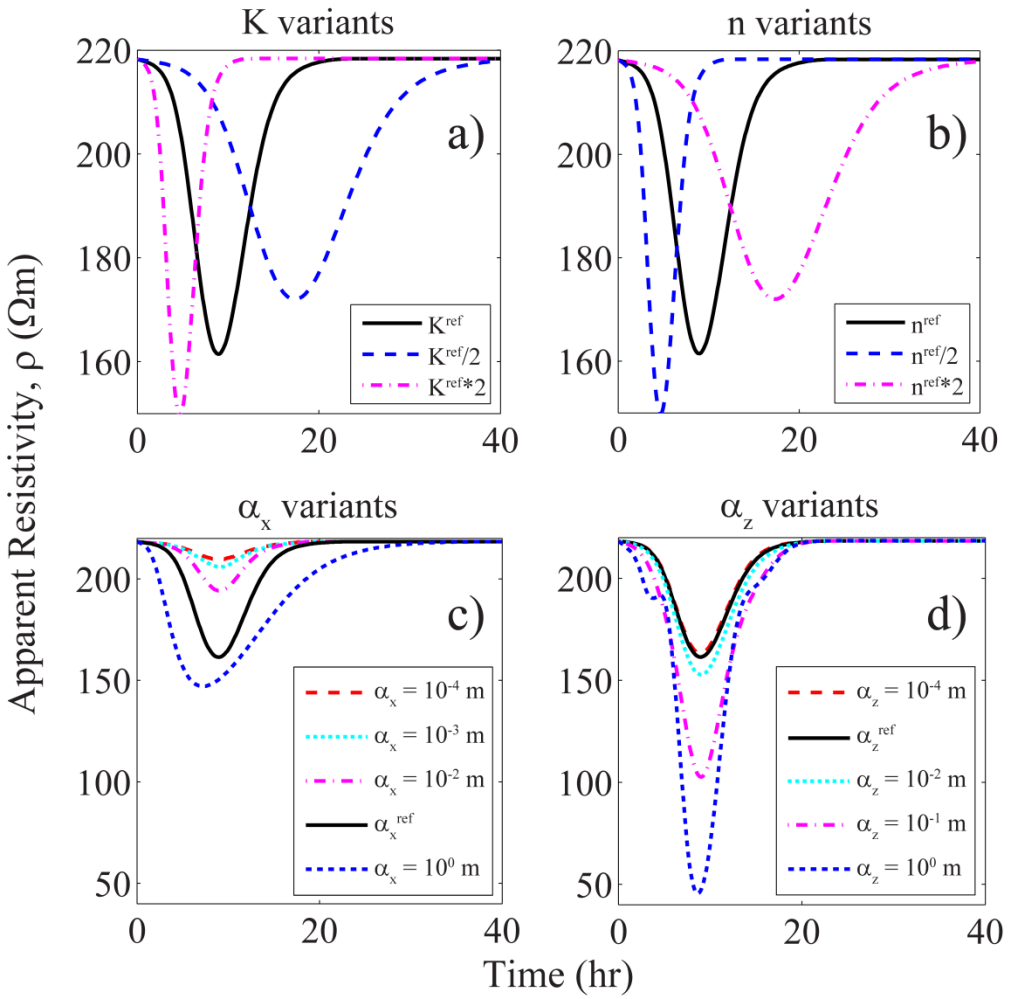

Figure 4.4: Apparent resistivity vs. time for variations in: a) K, b) n, c) α_x, and d) α_z. Each plot shows the reference homogeneous case with the solid black line. The dashed lines in (a) and (b) are variations by a factor of two. The dashed lines in (c) and (d) are variations in factors of 10, where the range is 10^{-4} to 10^{0} m for both α_x and α_z.

Figure 4.5 shows the ρ_{app} versus time for the heterogeneous Model A (a) and B (b) reference data and the PEST fit using Model C displayed by the green circle markers and the dashed line(s) respectively. In Figure 4.5b, the black and blue dashed lines correspond to the model design where $\alpha_z = 0.01\alpha_x$ and where α_z and α_x are untied respectively. The use of both tied and untied α-values is of special note here in Figure 4.5b, because the tied α-value model was wholly unable to produce the large magnitude change in the ρ_{app} signal that was seen in the Model B reference case, therefore the PEST optimization was conducted again using untied dispersivity values.

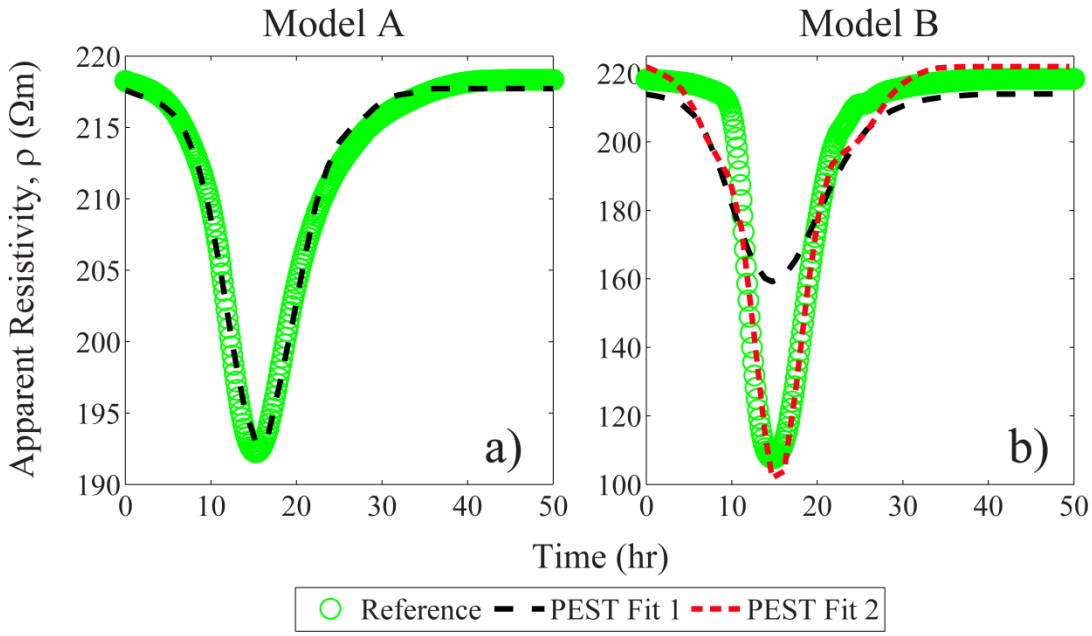

Figure 4.5: Apparent Resistivity vs. time for heterogeneous model PEST fits using the homogeneous Model C. Model A (a) data was fit using the relationship $\alpha_z = 0.01\alpha_x$ and Model B (b) data was fit using both $\alpha_z = 0.01\alpha_x$ and with α_x and α_z are untied. The dashed black and blue lines correspond to the tied and untied α_x-α_z relationship respectively.

Table 4.2 contains the PEST run statistics for the heterogeneous Model A and B data fitting using homogeneous Model C for the single current electrode pair case (both the tied and untied α_z to α_x tests for Model B). The statistics include the sum of squared

apparent resistivity differences (SSρD) for each pair as well as the RMSE for each pair. PEST output the SSρD for each test, whereas the RMSE was calculated using Equation 4.12.

Table 4.2: PEST run statistics for the data fit of Model's A and B using Model C including the PEST output of SSρD and the RMSE.

Model Tested	Test Type, #	CE Pair #	PEST SSρD	RMSE (Ωm)
Model A	single pair	1	23.2	0.79
Model B	single pair, test 1	1	12037	18.04
	single pair, test 2	1	1846	7.06

The results for the Model A PEST fit are a SSρD of 23.20 and when the SSρD for each pair in the multiple pair case are split, the values for CE pair # 1 and # 3 are slightly larger than the single pair case, but the value for CE pair # 2 is over a multiple of ten larger. The RMSE is around 0.79 Ωm. The results for the Model B PEST fit are a SSρD of 12040 and 1846 for test 1 and test 2 respectively where test 1 has a very poor data fit with the magnitude of the maximum ρ_{app} response about 50 Ωm greater than the reference maximum ρ_{app} and a RMSE of 18.04 Ωm. The RMSE for test 1 and test 2 are 18.04 and 7.06 Ωm respectively.

Table 4.3 contains the PEST parameter estimates for Model A and B data fits using Model C with corresponding 95% confidence intervals determined by PEST using the one current pair reference data sets. The results for each run include either estimates for K, n, and α_x for Model A and Model B - test 1 where α_z was tied to α_x by $\alpha_z = 0.01\alpha_x$ and K, n, α_x, and α_z for Model B - test 2 where the two dispersivities are untied.

Table 4.3: PEST results for Model A and B data fits using Model C. Parameter estimates and corresponding 95% confidence intervals determined by PEST. Parameter estimates include K, n, and α_x for Model A and Model B - test 1 where α_z was tied to α_x by $\alpha_z = 0.01\alpha_x$ and K, n, α_x, and α_z for Model B - test 2 where the two dispersivities are untied.

Model Tested	Test Type, #	Parameter	Estimate ± 95% Confidence Interval	Units
Model A	single pair	K	$5.62 \times 10^{-5} \pm 0.07 \times 10^{-5}$	m/s
		α_x	$1.93 \times 10^{-2} \pm 0.13 \times 10^{-2}$	m
		n	0.30 ± 0.0004	vol/vol
Model B	single pair, test 1	K	$5.89 \times 10^{-5} \pm 1.32 \times 10^{-5}$	m/s
		α_x	$1.69 \times 10^{-1} \pm 11.19 \times 10^{-1}$	m
		n	0.30 ± 0.0075	vol/vol
	single pair, test 2	K	$5.56 \times 10^{-5} \pm 0.15 \times 10^{-5}$	m/s
		α_x	$5.53 \times 10^{-2} \pm 1.76 \times 10^{-2}$	m
		α_z	$2.29 \times 10^{-1} \pm 0.41 \times 10^{-1}$	m
		n	0.30 ± 0.003	vol/vol

The results of PEST optimizations (i.e. estimation of parameters for Model C using data generated from Model A and B) for Model A and Model B (Figure 4.5, Table 4.2, and Table 4.3) indicate that through variations in K/n, α_x, and α_z the ρ_{app} curves for each case can be fit reasonably well, with the exception of the first test of Model B that has $\alpha_z = 0.01\alpha_x$. There is a moderate deviation at late (and early times with the Model B fit) times due to the tracer time lag in Model's A and B due to the vertical movement of the tracer around the low-K inclusion. This vertical movement does not occur in Model C.

The high SSρD and RMSE (Table 4.2) and very low confidence in the K and α-estimates in Model B - test 1, 22% and 662% of the estimated values respectively, indicate a very poor fit as can be seen in Figure 4.5b. The untying of α_x and α_z in Model B - test 2 facilitated the magnitude increase and shape change that were required to fit the

data generated using Model B using Model C. While the fit for Model B - test 2 is not obviously unacceptable due to the reasonable shape and magnitude of the ρ_{app} response, the ratio of the dispersivities (α_x/α_z) is 0.24, which indicates that α_z is approximately four times larger than α_x. This ratio is far less than commonly cited values in the literature, e.g., $\alpha_x/\alpha_z \cong 100$ [Gelhar et al., 1992].

4.5 Discussion

The results indicate that there can be erroneous outcomes in the coupled inversion using an incorrect hydrologic conceptual model. For instance, the homogeneous sensitivity analysis showed that a wide range of ρ_{app} magnitudes and durations can be attained from a fairly narrow adjustment to the hydrologic input parameters. Providing that the shape of the ρ_{app} signal is generally bell-shaped, which it was for Models A and B, it will be difficult to discriminate between homogeneous and heterogeneous conceptual models based on resistivity data alone. This example has shown that additional data (geophysical, hydrologic, and/or chemical) may be required to assess characteristics of an aquifer correctly.

There are a couple of geophysical methods that could be considered for further constraining the problem. Gathering more observational data by including additional current and potential electrode pairs that will further track the tracer's path and sample at different depths will help to refine the problem. Also, using GRP or seismic imaging can assist in construction of the aquifers structural model, which may include the low permeability zone.

This discussion will focus on the increasing the observational data by including two additional current-potential pairs. The two additional current pairs chosen for this investigation have 1) the same AB spacing with the center shifted to towards the downstream side of the model by 2.5m and 2) the same center with the AB spacing reduced by half to 5m. The purpose of the center-shifted pair is to track the tracer's movement downstream from the original pair. Likewise, the purpose of the spacing-reduced pair is to sample at less depth than the original pair. A schematic of the current electrode positions are displayed in Figure 4.6. The reference ρ_{app} curves for Model's A and B using the three current electrode pairs, CE pairs # 1 – 3, are generated using the same methodology as the previous analysis using only a single current pair.

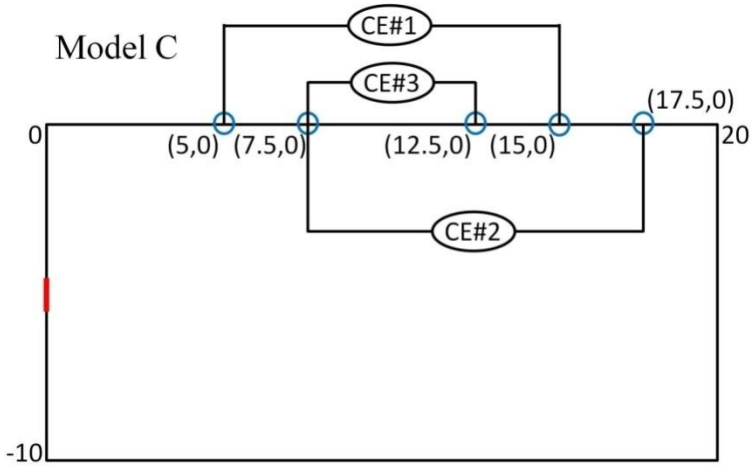

Figure 4.6: Model C showing the original current electrode position (CE pair #1) and the two new current electrode positions (CE pair #2 and CE pair #3).

Figure 4.7 shows the reference ρ_{app} versus time for the original current electrode pair location, CE pair # 1, in addition to the two new current pair locations, CE pair # 2 and # 3 for both heterogeneous Model A (a) and B (b). The blue circle, red square, and black diamond correspond to CE pair # 1, # 2, and # 3 respectively. The wavy pattern

between 20 and 25 hours in (b) is an artifact of the numerical instability caused by the extreme differences between the pore velocities at the end of the high-velocity chute.

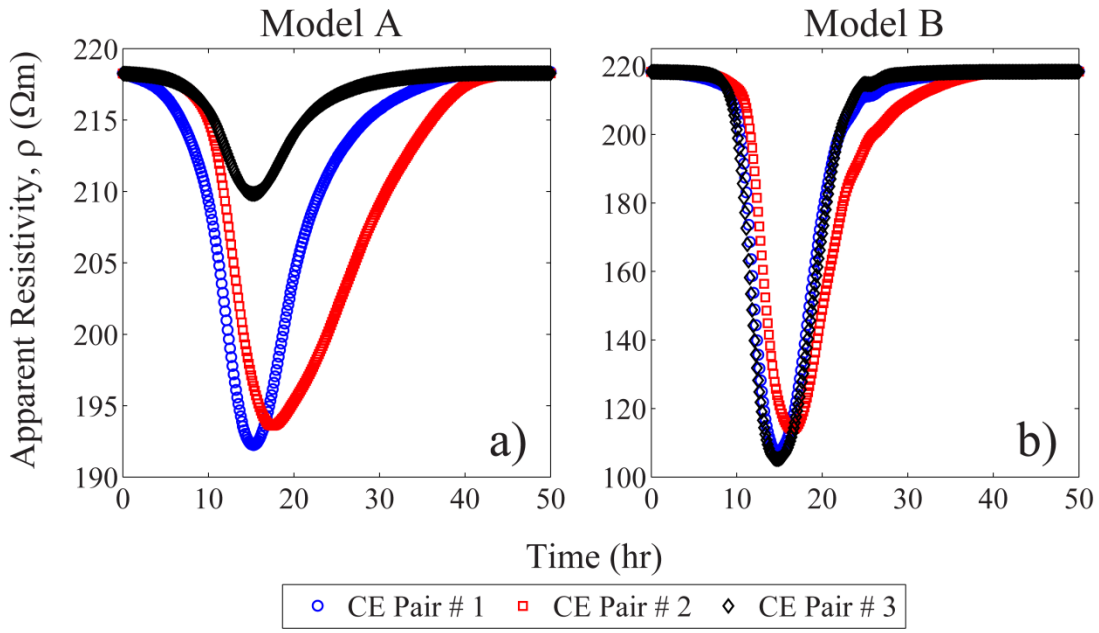

Figure 4.7: Apparent Resistivity vs. time for all three reference current electrode pairs for each heterogeneous Model A (a) and B (b).

Figure 4.8 shows the PEST curve fits for the ρ_{app} versus time for the estimation that contains all three current electrode pair positions (CE pair # 1 - # 3). The data fit for Model A and B are shown 4.8a-c and 4.8d-f respectively. CE pair # 1, # 2, and # 3 corresponds to 4.8a/d, 4.8b/e, and 4.8c/f respectively. The curves for the reference data and PEST fits correspond to the green circle markers and the black dashed lines respectively.

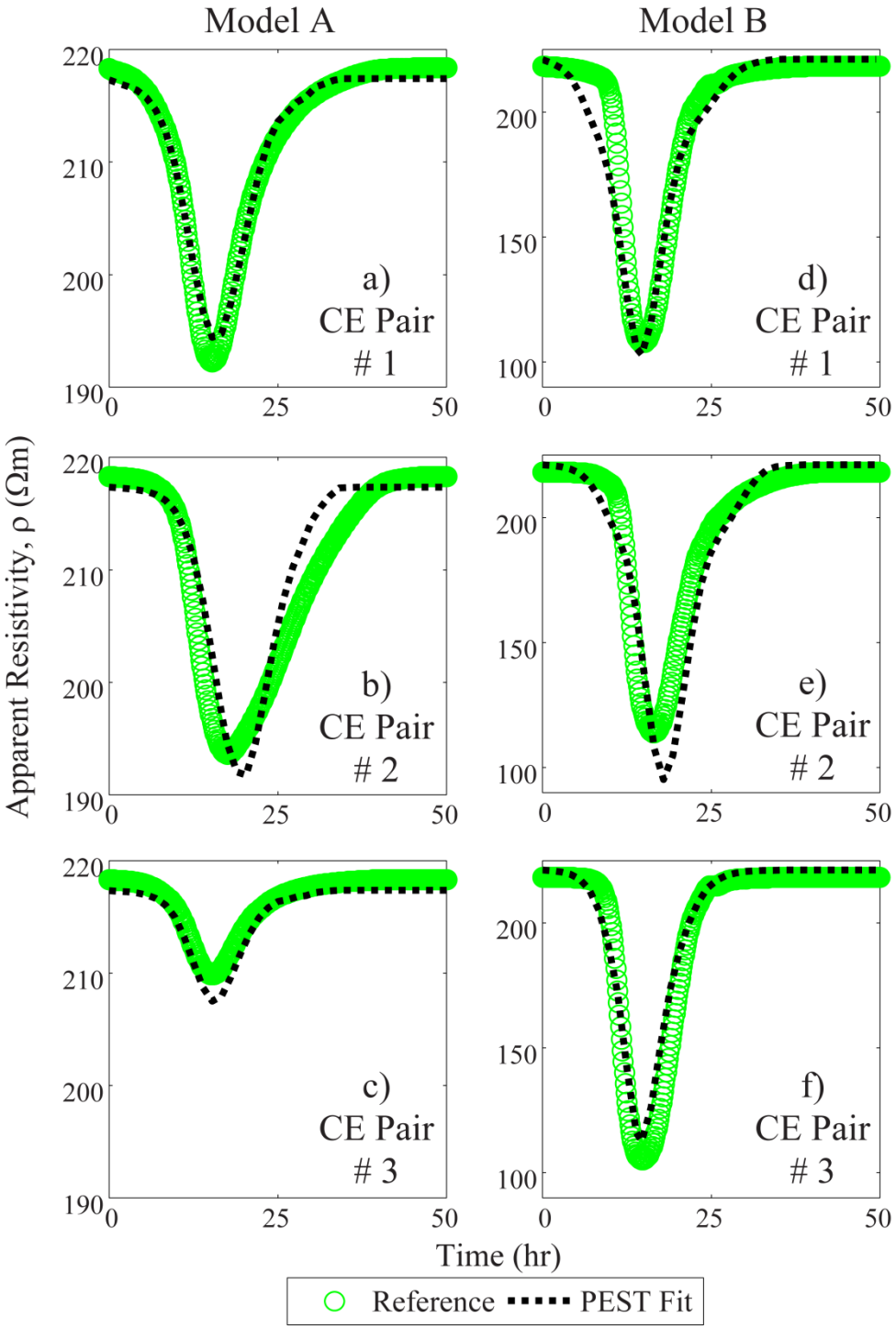

Figure 4.8: Apparent resistivity vs. time of heterogeneous Model A (a-c) and Model B (d-f) for each current pair (a-c and d-f correspond to CE pair #1 – CE pair #3 for each Model). The model reference and PEST fit are displayed by the circle and dashed lines respectively.

Table 4.4 contains the PEST run statistics for the heterogeneous Model A and B data fitting using homogeneous Model C for the three current electrode pair case. The statistics include the sum of squared apparent resistivity differences (SSρD) for the multiple-pair tests contain the combined SSρD, the split SSρD for each current pair, as well as the RMSE for each pair. The multiple-pair PEST runs were conducted using data from all pairs in the residual calculation. PEST output the SSρD for each pair and the combined SSρD, whereas the RMSE was calculated using Equation 4.12.

Table 4.4: PEST run statistics for the data fit of Model's A and B using Model C including the PEST output of SSρD and the RMSE.

Model Tested	Test Type	CE Pair #	PEST SSρD	PEST SSρD for Each Pair	RMSE for Each Pair (Ωm)
Model A	Multiple Pair	1	397.5	35.21	0.98
		2		316.4	2.92
		3		45.9	1.11
Model B	Multiple Pair	1	11194	3590	9.85
		2		5206	11.86
		3		2398	8.05

The result for the Model A PEST fit is an SSρD of 397.5. When the SSρD for each pair in the multiple pair case are split, the values for CE pair # 1 and # 3 are slightly larger than the single pair case (Table 2.2), but the value for CE pair # 2 is over a multiple of ten larger. The RMSE for each pair in both the single pair (Table 2.2) and multiple pair runs is around 1 Ωm with the exception of CE pair # 2, which has an RMSE of 2.92 Ωm. The result for the Model B PEST fit is an SSρD of 11190. When the SSρD for each pair in the multiple pair case are split, the values for CE pair # 1 and # 3 are

between 30 and 95% larger than the single pair, test 2 case (Table 2.2), and the value for CE pair # 2 is just over 180% larger. The RMSE for each pair ranges between 7.09 and 11.9 Ωm.

Table 4.5 contains the PEST parameter estimates for Model A and B data fits using Model C with corresponding 95% confidence intervals determined by PEST using the three current pair reference data sets. The results for each run include either estimates for K, n, and α_x for Model A where α_z was tied to α_x by $\alpha_z = 0.01\alpha_x$ and or estimates for K, n, α_x, and α_z for Model B, where the dispersivities are untied.

Table 4.5: PEST results for Model A and B data fits using Model C. Parameter estimates and corresponding 95% confidence intervals determined by PEST for the three current pair reference data sets. Parameter estimates include K, n, and α_x for Model A where α_z was tied to α_x by $\alpha_z = 0.01\alpha_x$ and K, n, α_x, and α_z for Model B - test 2 where the two dispersivities are untied.

Model Tested	CE Pairs	Parameter	Estimate ± 95% Confidence Interval	Units
Model A	3	K	$5.65 \times 10^{-5} \pm 0.09 \times 10^{-5}$	m/s
		α_x	$1.63 \times 10^{-2} \pm 0.21 \times 10^{-2}$	m
		n	0.30 ± 0.0004	vol/vol
Model B	3	K	$5.92 \times 10^{-5} \pm 0.13 \times 10^{-5}$	m/s
		α_x	$7.54 \times 10^{-2} \pm 1.78 \times 10^{-2}$	m
		α_z	$1.73 \times 10^{-1} \pm 0.21 \times 10^{-1}$	m
		n	0.30 ± 0.002	vol/vol

The results of including the two additional pairs (Figure 4.8a-f, Table 4.4, and Table 4.5) indicate that once there is enough data generated, the homogeneous model is unable to replicate the observations from each of the heterogeneous models as well. The largest error, both timing and magnitude errors combined, is produced by CE pair #2 for each optimization, as seen in Figure 4.8b/e. The reason for the increased error is that the

center of CE pair #2 is located at the downstream edge of the low-*K* block. At this point, which is also at the end of the high velocity chute, the vertical flow begins again and forces the tracer towards the center of the system causing rapid dispersion. On the whole, the other current pairs for each optimization have a good fit to the shape and magnitude of the reference data, which could be misleading with the exclusion of CE pair #2.

4.6 Conclusions

Though the reference cases, Model A and B, are quite extreme in the way that they force the tracer towards or away the surface rapidly over a short distance, in nature the differences would be much more subtle, it has shown that using IDF for hydrogeophysical interpretations can be misleading. The presence of a small low-*K* zone not unlike the heterogeneous examples (i.e. fold, dike, clay lens) could possibly cause problems for near-surface hydrogeophysical researchers. In a general attempt to shed light on this potential predicament, both synthetic homogeneous and heterogeneous simulations were conducted. In essence, there were several main points to take away from these experiments.

Problems can arise when using only a limited number of current pairs if the tracer is forced away from the surface by a low-hydraulic conductivity zone. This causes the magnitude of the apparent resistivity response to be less than it would if the tracer followed a path parallel to the surface. In this instance, an IDF optimization using an incorrect model concept (homogeneous in this case) will indicate that the dispersivities are much lower than they actually are.

When the tracer is forced towards the surface, the magnitude of the resulting apparent resistivity change is much greater than would be expected from a homogeneous system. In this case, the uncoupling of dispersivities is required to attain a fit, thus causing the estimated values to be somewhat unrealistic.

The problems that can arise when characterizing a heterogeneous system may be averted if 1) the researcher already has a good idea about the distributions of hydrologic facies or 2) many current pairs are utilized.

4.7 References

Archie, G. E. (1942), The electrical resistivity log as an aid in determining some reservoir characteristics, *Trans. Am. Inst. Min. Metall. Pet. Eng*., 146, 54– 62.

Bear, J. (1979), *Hydraulics of groundwater*, McGraw Hill, New York, 569 p.

Comsol Multiphysics 3.5a: User's Guide (2008), www.comsol.com.

Darcy, H. (1856), *Les fontaines publiques de la ville de Dijon*. Paris: Victor Dalmont.

Doherty, J. 2004. PEST: Model-Independent Parameter Estimation. *User Manual* (5th ed). Corinda, Queensland, Australia: Watermark Numerical Computing.

Ferre, T., L. Bentley, A. Binley, N. Linde, A. Kemna, K. Singha, K. Holliger, J. A. Huisman, B. Minsley (2009), Critical steps for the continuing advancement of hydrogeophysics, *EOS Trans. AGU*, vol. 90, no. 23, pp. 200.

Fetter, C.W. (2001), *Applied hydrogeology*. Prentice Hall, Upper Saddle River, N.J., 4th Ed., 598p.

Freeze, R. A., J. A. Cherry (1979), *Groundwater*. Prentice Hall, Englewood Cliffs, N.J., 604p.

Gaganis, P., L. Smith (2001), A Bayesian approach to the quantification of the effect of model error on the predictions of groundwater models, *Water Resources Research*, vol. 37, no. 9, pp. 2309-2322.

Gaganis, P., L. Smith (2006), Evaluation of the uncertainty of groundwater model predictions associated with conceptual errors: A per-datum approach to model calibration, *Advances in Water Resources*, vol. 29, no. 4, pp. 503–514.

Gelhar, L. W. , C. Welty, K. R. Rehfeldt (1992), A critical review of data on field-scale dispersion in aquifers, *Water Resources Research*, vol. 28, no. 7, pp. 1955-1974.

Hinnell, A. C. , T. P. A. Ferre, J. A. Vrugt, J. A. Huisman, S. Moysey, J. Rings, M. B. Kowalsky (2010), Improved extraction of hydrologic information from geophysical data through coupled hydrogeophysical inversion, *Water Resources Research*, vol. 46, W00D40.

Lambot, S., E. C. Slob, M. Vanclooster, H. Vereecken (2006), Closed loop GPR data inversion for soil hydraulic and electric property determination, *Geophysical Research Letters*, vol. 33, no. 21, L21405.

Lesmes, D. P., S. P. Friedman (2005), Relationships between the electrical and hydrogeological properties of rocks and soils, In: Rubin, Y, S. S. Hubbard (eds) *Hydrogeophysics, Chapter 4*, Springer, Dordrecht, The Netherlands, pp 87–128.

Moysey S., R. J. Knight, K. Singha (2006), Relating geophysical and hydrologic properties using field-scale rock physics, *CMWR XVI -- Computational Methods in Water Resources*, Copenhagen, Denmark, 8p.

Wenner, F. (1912a), The four-terminal conductor and the Thompson Bridge, *U. S. Bureau of Standards Bulletin*, vol. 8, pp. 559-610.

Wenner, F. (1912b), A method of measuring earth resistivity, *U. S. Bureau of Standards Bulletin*, vol. 12, pp. 469-478.

CHAPTER 5

CONCLUSIONS

Traditional saturated zone methods can be invasive, costly with regard to time and money, and often can lead to inadequate sampling of spatial heterogeneities. Surface resistivity methods can be used in addition to traditional methods to gain better spatial resolution for near-surface aquifer characterization. This research set out to be a theoretical segue into a multiphysics modeling technique that utilizes limited surface resistivity data for saturated zone hydrologic model calibration and parameter estimation. To that end, an examination of integrated data fusion (IDF) was conducted to determine what common trends occur within the modeling environment.

Firstly, in an optimization of hydraulic conductivity (K) within a homogeneous system, IDF has shown that good estimations of hydraulic conductivity can be attained using IDF with only limited resistivity data. The data collection method must take into account some prior information about the aquifer, as seen with the lack of a sufficient sampling rate that missed the migrating plume (Chapter 2, Optimization). Also examined was the ability of the IDF scheme as it relates to the ability to delineate K with variations in tracer concentration, injection depth, and noise in voltages (Chapter 2, Sensitivity Analysis). It was shown that the ability to estimate K increases with increasing tracer concentration, decreasing injection depth, and decreasing background noise. The resultant trends indicate that one must take into the survey design conditions such as background noise and the tracer injection depth before selecting a tracer concentration.

Secondly, an examination of the sensitivity of IDF to variations in *K*, porosity (*n*), and dispersivity (α) was conducted. It was determined that *K* and n are quite sensitive to the flow velocity as given by Darcy's Law and good *K*/*n* estimates can be gained by using the maximum resistivity response only. With the dependence of n to Archie's Law in the equation system and a point sample of background concentration, the trade-off between *K* and *n* can be overcome. Unlike the *K*/*n* dependence to velocity, α is much more difficult to constrain because of the non-uniqueness of the apparent resistivity to α when only one current electrode pair is used. Hence, it is has been found that more than a single current pair be used when accurate estimates of α are desired.

Lastly, the question of whether or not determination of an incorrect conceptual model is within the IDF scheme's ability. To examine this question, two diametrically opposite synthetic systems that either forces the tracer towards or away from the surface electrodes are used to generate synthetic data. This data was then used in an IDF optimization using a homogeneous model and PEST to determine if the data could be fit. It was shown that when there is a lower magnitude of the maximum voltage response, the homogeneous model fit the data acceptably by reducing the values of α. When there is a higher magnitude of the maximum response, the homogeneous model is unable to replicate the data in a realistic fashion. Thus, it is shown that due to this non-uniqueness there is a potential for erroneous results using IDF and a single pair of current electrodes. To test this, two additional current electrode pairs were included in the optimization and it was shown with the addition of extra pairs, it was more difficult to fit the data.

5.1 Recommendations for Future Work

Future work on inverting resistivity data using IDF should include an examination into what magnitudes of current injection for various systems will be the most effective. It is suggested that all of the synthetic analyses be replicated in lab-scale experiments to determine the efficacy of this method. A lab-scale survey should also be conducted with a partially saturated vadoze zone to determine the effects of its inclusion on the ability to estimate hydrologic parameters using sparse resistivity data.